

# Strength and challenges for transient mid to late Holocene simulations with dynamical vegetation

Pascale Braconnot\*, Dan Zhu, Olivier Marti and Jérôme Servonnat

IPSL/Laboratoire des Sciences du Climat et de l'Environnement, unité mixte CEA-CNRS-UVSQ, Université Paris Saclay, Bât. 714, Orme de Merisiers, 91191 Gif-sur-Yvette Cedex.

*Correspondance to* : pascale.braconnot@lsce.ipsl.fr

**Abstract.** We present the first simulation of the last 6000 years with a version of the IPSL Earth System model that includes interactive dynamical vegetation and carbon cycle. It is discussed at the light of a set of mid Holocene and pre industrial simulations performed to set up the model version and to initialize the dynamical vegetation. These sensitivity experiments remind us that model quality or realism is not only a function of model parameterizations and tuning, but also of experimental set up. The transient simulations shows that the long term trends in temperature and precipitation have similar shape to the insolation forcing, except at the equator, in high latitudes and south of 40° S. In these regions cloud cover, sea-ice, snow, or ocean heat content feedbacks lead to smaller or opposite temperature responses. The long term trend in tree line in northern hemisphere is reproduced and starts earlier than the southward shift vegetation over the Sahel. Despite little change in forest cover over Eurasia, a long term change in forest composition is simulated, including large centennial variability. The rapid increase of atmospheric CO<sub>2</sub> in the last centuries of the simulation contributes to enhance tree growth and counteracts the long term trends induced by Holocene insolation in the northern hemisphere and amplify it in the southern hemisphere. We also highlight some limits in the evaluation of such a simulation resulting from model climate-vegetation biases, the difficulty to fully assess the result for pre-industrial or modern conditions that are affected by land-use, and the possibility for multi-vegetation state under modern conditions.

## 1 Introduction

Past environmental records such as lake levels or pollen records highlight substantial changes in the global vegetation cover during the Holocene (COHMAP-Members, 1988; Wanner et al., 2008). The early to mid-Holocene optimum period was characterized by a northward extension of boreal forest over north Eurasia and America which attests for increased temperature in mid to high latitudes (Prentice and Webb, 1998). A massive expansion of moisture and precipitation in Afro-Asian regions has been related to enhance boreal summer monsoon (Jolly et al., 1998; Lezine et al., 2011). These changes were triggered by latitudinal and seasonal changes in top of the atmosphere (TOA) incoming solar radiation caused by the long term variation in Earth's orbital parameters (Berger, 1978). During the course of the Holocene these features retreated towards their modern distribution (Wanner et al., 2008). While global data syntheses exist for the mid-Holocene (Bartlein et al., 2011; Harrison, 2017; Prentice et al., 2011), reconstructions focus in general on a location or a region when considering the whole Holocene. For example regional syntheses for long term paleo records over Europe reveal long term vegetation changes that can be attributed to changes in temperature or precipitation induced by insolation changes (Davis et al., 2003; Mauri et al., 2015). Similarly, over West Africa or Arabia, pollen data suggests a southward retreat of the intertropical convergence zone (Lezine et al., 2017), and a reduction in North

37 African monsoon intensity (Hély and Lézine, 2014). The pace of these changes varies from one region to the  
38 other (e.g. Fig. 6.9 in Jansen et al., 2007; Renssen et al., 2012) and has been punctuated by millennium scale  
39 variability or abrupt events (deMenocal et al., 2000), for which it is still unclear that they represent global or  
40 more regional events. How vegetation changes have been triggered by this long term climate change and what  
41 has been the vegetation feedback on climate is still a matter of debate.

42 Pioneer simulations with asynchronous climate-vegetation coupling highlighted that vegetation had a  
43 strong role in amplifying the African monsoon (Braconnot et al., 1999; Claussen and Gayler, 1997; de Noblet-  
44 Ducoudre et al., 2000; Texier et al., 1997). When dynamical vegetation models were included in fully coupled  
45 ocean-atmosphere-sea-ice models, climate simulations suggested a lower magnitude of the vegetation feedback  
46 (Braconnot et al., 2007a; Braconnot et al., 2007b; Claussen, 2009). Individual model results indicate however  
47 that vegetation plays a role in triggering the African monsoon during the mid-Holocene (Braconnot and  
48 Kageyama, 2015), but also that soil moisture might play a larger role than anticipated (Levis et al., 2004).  
49 Reduced dust emission with increased vegetation and changed soil properties have been shown to amplify  
50 monsoon changes (Albani et al., 2015; Egerer et al., 2017; Pausata et al., 2016). In high latitude as well, the role  
51 of the vegetation feedback is not fully understood. Previous studies showed that the response of vegetation in  
52 spring combined to the response of the ocean in autumn were key factors to transform the seasonally varying  
53 insolation forcing into an annual mean warming (Wohlfahrt et al., 2004). The magnitude of this feedback has  
54 been questioned by Otto et al. (2009), showing that vegetation was mainly responding to the ocean and sea-ice  
55 induced warming over land. The role and magnitude of the vegetation feedback were also questioned over Asia  
56 (Dallmeyer et al., 2010). The variety of response of dynamical vegetation models to external forcing is an issue  
57 in these discussions. However they all produce increased vegetation in Sahel when forced with mid-Holocene  
58 boundary conditions, which suggests that, despite large uncertainties, robust basic response can be inferred from  
59 current models (Hopcroft et al., 2017). Other studies have highlighted that there might exist several possible  
60 vegetation distribution at the regional scale for a given climate that can be related to instable vegetation states  
61 (e.g. Claussen, 2009). This is still part of the important questions to solve to fully explain the end of the African  
62 humid period around 4000-5000 years BP (Liu et al., 2007).

63 It is not clear yet that more comprehensive models and long Holocene simulations can help solve all the  
64 questions, given all the uncertainties described above. But they can help to solve the question of vegetation-  
65 climate state and of the linkages between insolation, trace gases, climate and vegetation changes at global and  
66 regional scales. For this, we investigate the last 6000 years long term trend and variability of vegetation  
67 characteristics as simulated by a version of the IPSL model with an interactive carbon cycle and dynamical  
68 vegetation. Offline simulations, using the original scheme for dynamical vegetation of ORCHIDEE, were  
69 already used to analyze Mid-Holocene and LGM vegetation (Kageyama et al., 2013b; Woillez et al., 2011). This  
70 has not yet been done in the fully coupled system for long transient simulations. Previous studies clearly  
71 highlight that small differences in the albedo or soil formulation can have large impact on the simulated results  
72 (Bonfils et al., 2001; Otto et al., 2011). Given all the interactions in a climate system, the climatology produced  
73 by a model version with interactive vegetation is by construction different from the one of the same model with  
74 prescribed vegetation. In particular model biases are in general larger (Braconnot and Kageyama, 2015;  
75 Braconnot et al., 2007b), so that the corresponding simulations need to be considered as resulting from different  
76 models (Kageyama et al., 2018). The way the external forcing is applied to the model can also lead to

77 climatology or vegetation differences between two simulations with the same model. It is thus important to know  
78 how the changes we made to the IPSL climate model to set up the version with dynamical vegetation affect the  
79 results and the realisms we can expect from the transient simulations. We thus investigate first how the major  
80 changes and tuning affect the mid-Holocene simulations and the performances of the model compared to  
81 simulations with the previous model version IPSLCM5A (Dufresne et al., 2013; Kageyama et al., 2013a).  
82 Several questions guide the analyses of the transient experiment. Is the long term response of climate and  
83 vegetation a direct response to the insolation forcing? How large is the impact of the trace gases? How different  
84 is the timing of the vegetation change in different regions? Do we need to care about variability over such a long  
85 time period? We also need to put the responses to these questions in perspective with the level of realism we can  
86 expect from the simulated vegetation in such a simulation. It concerns the model biases, the compatibility  
87 between the climate and vegetation states produced by the transient simulation or obtained from snap shot  
88 experiments. Also different strategies can be used to initialize the vegetation dynamics and produce the mid-  
89 Holocene initial state for the transient simulation. We investigate if they have an impact on the simulated  
90 vegetation distribution.

91 The remainder of the manuscript is organized as follow. Section 2 describes the experimental set up, the  
92 characteristics of the land surface model as well as different model adjustments we made, and the initial state for  
93 the dynamical vegetation. Section 3 presents the transient simulation focusing on long term climate and  
94 vegetation trends at global and regional scales. Section 4 discusses the realism of the simulated vegetation and  
95 different sources of uncertainties that can affect it, before the conclusion presented in section 5.

## 96 **2 Model and the suite of experiments**

### 97 **2.1 Experimental design**

98 The mid-Holocene (MH) time-slice climate experiment (6000 years BP) represents the initial state for  
99 the last 6000 years transient simulation with dynamical vegetation. It is thus considered as a reference climate in  
100 this study. Because of this, and to save computing time, model adjustments made to set up the model content and  
101 the model configuration were mainly done running MH and not pre-industrial (PI) simulations (Table 1 and 2).  
102 Only a subset of PI simulation is available for comparison with modern conditions. All the simulations were run  
103 long enough (300-1000 years) to reach a radiative equilibrium and be representative of a stabilized MH climate  
104 (Fig. 1). They are free of any artificial long term trends after the adjustment phase, as were IPSL PMIP3 MH  
105 simulations (Fig. 1, Kageyama et al., 2013a).

106 Most tests follow the MH PMIP3 protocol (Braconnot et al., 2012). This is only due to the fact that this  
107 work began before the PMIP4 boundary conditions were available. But the transient simulation (TRHOLV, for  
108 TRansient HOlocene simulation with dynamical Vegetation), and the 1000 year-long MH simulations with or  
109 without dynamical vegetation that were run to prepare the initial state for it, follows the PMIP4-CMIP6 protocol  
110 (Otto-Bliesner et al., 2017, Tab. 1). In all simulations the Earth's orbital parameters are derived from Berger  
111 (1978). The MH PMIP3 protocol uses the trace gases (CO<sub>2</sub>, CH<sub>4</sub> and N<sub>2</sub>O) reconstruction from ice core data by  
112 Joos and Spahni (2008). It has been updated for PMIP4, using new data and a revised chronology that provides  
113 a consistent history of the evolution of these gases across the Holocene (Otto-Bliesner et al., 2017). The  
114 difference in forcing between PMIP4 and PMIP3 was estimated to be  $-0.8 \text{ W m}^{-2}$  by Otto-Bliesner et al. (2017).

115 This is the order of magnitude found for the imbalance in net surface heat flux at the beginning of the MH-  
116 FPMIP4 simulation. This simulation started from L11Aer run with PMIP3 protocol (Fig. 1a). It uses the same  
117 model version, but follows the PMIP4 protocol. For the subset of PI experiments Earth's orbit and trace gases  
118 are prescribed to year 1860, i.e. the beginning of the industrial area. For the MH and PI time slice experiments,  
119 boundary conditions do not vary with time. For the transient simulations the Earth's orbital parameters and trace  
120 gases are updated every year.

121 In standard versions of the IPSL model, aerosols are accounted for by prescribing the optical  
122 distribution of dust, sea-salt, sulfate and particulate organic matter (POM), so as to take into account the  
123 coupling between aerosols and radiation (Dufresne et al., 2013). For MH simulations these variables are  
124 prescribed to 1860 CE values, for which the level of sulfate and POM is slightly higher than the values found in  
125 the Holocene (Kageyama et al., 2013a). Here, except for the first few tests (Tab. 1), we prescribe only dust and  
126 sea-salt to their 1860 values and neglect the other aerosols. A fully coupled dust-sea salt-climate version of the  
127 model that does not consider the other aerosols is under development for long transient simulations. For future  
128 comparisons it is important to have similar model set up. Indeed, compared to the version with all aerosols,  
129 considering only dust and sea salts imposes a radiative difference of about  $2.5 \text{ W m}^{-2}$  in external climate forcing.  
130 Its footprint appears on the net heat flux imbalance at the beginning of L11Aer. It leads to a global air  
131 temperature increase of  $1.5 \text{ }^\circ\text{C}$  (Fig. 1c). The largest warming over land is found in the northern hemisphere, but  
132 the ocean warms almost everywhere by about  $1 \text{ }^\circ\text{C}$ , except in the Antarctic circumpolar current (Fig. 2a). The  
133 warmer conditions favor higher precipitation with a global pattern rather similar to what is found in future  
134 climate projections (Fig. 2b). This offset affects the mean climate state and is larger than the expected effect of  
135 Holocene dusts.

## 136 **2.2 The IPSL Earth System Model and updated version of the land surface scheme**

137 For these simulations, we use a modified version of the IPSLCM5A model (Dufresne et al., 2013). This  
138 model version couples the LMDZ atmospheric model with  $144 \times 142$  grid points in latitude and longitude  
139 ( $2.5^\circ \times 1.27^\circ$ ) and 39 vertical levels (Hourdin et al., 2013) to the ORCA2 ocean model at  $2^\circ$  resolution (Madec,  
140 2008). The ocean grid is such that resolution is enhanced around the equator and in the Arctic due to the grid  
141 stretching and pole shifting. The LIM2 sea-ice model is embedded in the ocean model to represent sea ice  
142 dynamics and thermodynamics (Fichefet and Maqueda, 1999). The ocean biogeochemical model PISCES is also  
143 coupled to the ocean physics and dynamics to represent the marine biochemistry and the carbon cycle (Aumont  
144 and Bopp, 2006). The atmosphere-surface turbulent fluxes are computed taking into account fractional land-sea  
145 area in each atmospheric model grid box. The sea fraction in each atmospheric grid box is imposed by the  
146 projection of the land-sea mask of the ocean model on the atmospheric grid, allowing for a perfect conservation  
147 of energy (Marti et al., 2010). Ocean-sea-ice and atmosphere are coupled once a day through the OASIS coupler  
148 (Valcke, 2006). All the simulations keep exactly the same set of adjusted parameters as in Dufresne et al. (2013)  
149 for the ocean-atmosphere system.

150 The land surface scheme is the ORCHIDEE model (Krinner et al., 2005). It is coupled to the  
151 atmosphere at each atmospheric model 30 min physical time steps and includes a river runoff scheme to route  
152 runoff to the river mouths or to coastal areas (d'Orgeval et al., 2008). Over the ice sheet water is also routed to  
153 the ocean and distributed over wide areas so as to mimic iceberg melting and to close the water budget (Marti et

154 al., 2010). This model accounts for a mosaic vegetation representation in each grid box, considering 13  
155 (including 2 crops) plant functional types (PFT) and interactive carbon cycle (Krinner et al., 2005).

156 We made several changes in the land-surface model (Tab. 1). The first one concerns the inclusion of the  
157 11 layer physically-based hydrological scheme (de Rosnay et al., 2002) that replaces the 2 layer bucket-type  
158 hydrology (Ducoudré et al., 1993). The 11 layer hydrological model had never been tested in the full coupled  
159 mode before this study. We gave specific care to the closure of the water budget of the land surface model to  
160 ensure that  $O(1000)$  years) simulations will not exhibit spurious drift in sea level and salinity. In addition the new  
161 prognostic snow model was included (Wang et al., 2013). The scheme describes snow with 3 layers that are  
162 distributed so that the diurnal cycle and the interaction between snowmelt and runoff are properly represented. In  
163 order to avoid snow accumulation on a few grid points, snow depth is not allowed to exceed 3m. The excess  
164 snow is melted and added to soil moisture and runoff while conserving water and energy (Charbit and Dumas,  
165 pers. communication). Because of a large cold bias in high latitudes in the first tests, we reduced the bare soil  
166 albedo that is used to combine fresh snow and vegetation in the snow aging parameterization. Other changes  
167 concern the adjustments of some of the parameterizations. The way the mosaic vegetation is constructed in  
168 ORCHIDEE favors too much bare soil when leaf area index (LAI) is low (Guimberteau et al., 2018). To  
169 overcome this problem, an artificial 0.70 factor was implemented in front of bare soil evaporation to reduce it  
170 (Table. 1). This factor is compatible with the order of magnitude of the reduction brought by the implementation  
171 of a new evaporation parametrization for bare soil in the current IPSLCM6A version of the model (Peylin pers.  
172 communication.). For all the other surface types the evaporation is computed as in L11. The last adjustment  
173 concerns the combination of snow albedo with the vegetation albedo. The procedure was different when  
174 vegetation was interactive or prescribed. Now, the combination of snow and vegetation albedo is based on the  
175 effective vegetation cover in the grid box in both cases. It leads to larger albedo than with the IPSL-CM5A-LR  
176 reference version when vegetation is prescribed. It counteracts the effect of the fresh snow albedo reduction.

### 177 **2.3 Impact of the different changes on model climatology and performances**

178 Figure 1 and 2 highlight how the changes discussed in section 2.2 affect the model adjustment and  
179 climatology. The hydrological model (L11) produces about  $1.25 \text{ mm.d}^{-1}$  higher global annual mean evaporative  
180 rates than MH PMIP3. The water cycle is more active in L11. Precipitation is enhanced in the mid-latitudes and  
181 over the tropical lands (Fig. 2c) where larger evapotranspiration and cloud cover both contribute to cool the land  
182 surface (Fig. 2d). A higher evaporative rate should lead to a colder global mean temperature (Fig. 1c). This is not  
183 the case. The large scale cooling over land is compensated by warming over the ocean (Fig. 2d), caused by  
184 reduced ocean evaporation and changes in the ocean-land heat transport. The radiative equilibrium is achieved at  
185 the top of the atmosphere with the same global mean long wave and short wave radiation budget in the two  
186 simulations (L11 and MH-PMIP3).

187 The factor introduced to reduce bare soil evaporation didn't lead to the expected reduction of  
188 evaporation (Fig 1b). Indeed, when evaporation is reduced, soil temperature increases and the regional climate  
189 gets warmer allowing for more moisture in the atmosphere and thereby more evaporation where soil can supply  
190 water (Fig. 2 e and f and Fig. 1). Therefore, differences resulting from bare soil evaporation do not show up on  
191 the precipitation map (Fig. 2e) but on the increased temperature over land in the northern hemisphere (Fig. 1f). It  
192 is consistent with similar findings when analyzing land use feedback (Boisier et al., 2012). Note that in Fig. 2f

193 about 0.1° C of the 0.4° C global warming in L11AerEv is still a footprint of the warming induced by the aerosol  
194 effect described in section 2.1, but that it doesn't alter our conclusions on the regional temperature-evaporation  
195 feedback.

196 The difference between MH-FPMIP4 and MH-PMIP3 represents the sum of all the changes in the land  
197 surface model and forcing discussed above (Fig. 2 g and h). A PI simulation performed with the new model  
198 version (PI-FPMIP4, Tab. 1) allows us to assess how they affect the model performances. A rapid overview of  
199 model performances is provided by a simple set of metrics derived from the PCMDI Metric Package (Gleckler et  
200 al., 2016, see appendix 1). Fig. 3 highlights that temperature biases are reduced in PI-FPMIP4 at about all model  
201 levels but that biases are enhanced for precipitation and total precipitable water compared to PI-PMIP3  
202 (comparison of blue and black lines in Fig. 3). Taken all together all the changes we made have little effect on  
203 the bias pattern (Fig. 3a). The model performs quite well compared to the CMIP5 ensemble of PI simulations,  
204 except for cloud radiative effect (Fig. 3). The effect of cloud in the IPSLCM5A-LR simulations results mainly  
205 from low level clouds over the ocean (Braconnot and Kageyama, 2015; Vial et al., 2013). The atmospheric  
206 tuning is exactly the same as in the default IPSLCM5A-LR version, and the introduction of all the changes  
207 described above have almost no effect on the cloud radiative effect. Overall the model version with the 11 layer  
208 hydrology has similar skill as the IPSLCM5A reference (Dufresne et al., 2013) and we are confident that the  
209 version is sufficiently realistic to serve as a basis on top of which we can include the dynamical vegetation.

#### 210 **2.4 Initialization of the mid-Holocene dynamical vegetation for the transient simulation**

211 We added the vegetation dynamics by switching on the dynamical vegetation model described in Zhu et  
212 al. (2015). Compared to the original scheme (Krinner et al., 2005), it produces more realistic vegetation  
213 distribution in mid and high latitude regions when compared with present-day observations.

214 Two different strategies have been tested to initialize the dynamical vegetation (Tab. 2). In the first case  
215 (MH-Vmap), the initial vegetation distribution was obtained from an off line simulation with the land surface  
216 model forced by CRU-NCEP 1901-1910 climatology. In the second case (MH-Vnone), the model restarted from  
217 bare soil with the dynamical vegetation switched on, using the same initial state as MH-Vmap for the  
218 atmosphere, the ocean, the sea-ice and the land-ice. As expected, the evolution of bare soil, grass and tree are  
219 very different between MH-Vmap and MH-Vnone during the first adjustment phase (black and blue curves in  
220 Fig. 4 a, b, and c). Vegetation adjusts in less than 100 years (1200 months) in MH-Vmap (blue curve). This short  
221 term adjustment indicates that the climate-vegetation feedback has a limited impact on vegetation when the  
222 initial state is already consistent with the characteristics of the simulated climate. In MH-Vnone that starts from  
223 bare soil (black curve), the adjustment has a first rapid phase of 50 years for bare soil and about 100 years for  
224 grass and tree, followed by a longer phase of about 200 years. The latter corresponds to a long term oscillation  
225 that has been induced by the initial coupling choc between climate and land surface. Note that PMIP4 instead of  
226 PMIP3 MH boundary conditions were used to run the last part of these simulations (red and yellow curves in  
227 Fig. 4 a, b, and c). In the coupled system, most of the vegetation adjustment takes about 300 years, which is  
228 longer than results of off line ORCHDEE simulations (less than 200 years). Since MH-Vnone started from a  
229 coupled ocean-atmosphere-ice state at equilibrium, this result also indicates that the land-sea-atmosphere  
230 interactions do not alter much the global energetics of the IPSL model in this simulation where atmospheric CO<sub>2</sub>  
231 is prescribed. The two simulations converge to very similar global vegetation cover. Figure 4 suggests that there

232 is only one global mean stable state for the mid-Holocene with the IPSL model, irrespective of the initial  
233 vegetation distribution (see also Tab. A2, appendix A2).

234 For the transient simulation, we decided to use the results of the MH-VNone simulation as initial state  
235 (Table 2), because it leads to more realistic forest in the PI-Vnone simulation (see discussion in section 4). We  
236 performed a preindustrial simulation (PI-Vnone) using MH-Vnone as initial state and switching on the orbital  
237 parameters and trace gases to their PI values. Figure 3 indicates that the vegetation feedback slightly degrades  
238 the global performances for PI temperature and bring the model performance close to the IPSLCM5A-LR  
239 CMIP5 version. It also contributes to reduce the mean bias in precipitable water, evaporation, precipitation and  
240 long wave radiation, but it has no effect on the bias pattern (assessed by the rmst in Fig. 3, see also appendix).  
241 Vegetation has thus an impact on climate, but its effect is of smaller magnitude than those of the different model  
242 and forcing adjustments done to set up the model version we use here. Section 4 provides a more in depth  
243 discussion of the vegetation state.

### 244 **3 Simulated climate and vegetation throughout the mid to late Holocene**

#### 245 **3.1 Long term forcing**

246 Starting from the MH-Vnone simulation the transient simulation of the last 6000 years (TRHOLV)  
247 allows us to test the response of climate and vegetation to atmospheric trace gases and Earth's orbit (see section  
248 2.1). The atmospheric CO<sub>2</sub> concentration is slowly rising throughout the Holocene from 264 ppm 6000 years ago  
249 to 280 for the pre-industrial climate around -100 BP (1850 CE) and then experiences a rapid increase from -100  
250 BP to 0 BP (1950 CE) (Fig. 5). The methane curve shows a slight decrease and then follows the same evolution  
251 as CO<sub>2</sub>, whereas NO<sub>2</sub> remains around 290 ppb throughout the period. The radiative forcing of these trace gases is  
252 small over most of the Holocene (Joos and Spahni, 2008). The largest changes occurred with the industrial  
253 revolution. The rapid increase in the last 100 years of the simulation has an imprint of about 1.28 W m<sup>-2</sup>.

254 The major forcing is caused by the slow variations of the Earth's orbital parameters that induce a long  
255 term evolution of the magnitude of the incoming solar radiation seasonal cycle at the top of the atmosphere (Fig.  
256 5). It corresponds to decreasing seasonality (difference between the maximum and minimum monthly values for  
257 each year) in the northern Hemisphere and increasing seasonality in the southern Hemisphere (Fig. 5). It results  
258 from the combination of the changes in summer and winter insolation in both hemispheres (Fig. 6). These  
259 seasonal changes are larger at the beginning of the Holocene (about -8 W m<sup>-2</sup> per millennia in the NH and  
260 +5 W m<sup>-2</sup> per millennia in the SH) and then the rate of change linearly decreases in the NH (increases in the SH)  
261 from 4500 to about 1000 years BP (Fig. 5). There is almost no change in seasonality in the NH over the last 1000  
262 years, whereas in the SH seasonality starts to decrease again by 2000 years BP. The shape of insolation changes  
263 is thus different in both hemisphere, and so is the relative magnitude of the seasonal cycle between the two  
264 hemispheres. This would be seen whatever the calendar we use to compute the monthly means because of the  
265 seasonal asymmetry induced by precession at the MH (see: Jousaume and Braconnot, 1997; Otto-Bliesner et al.,  
266 2017).

## 267 3.2 Long term climatic trends

268 Changes in temperature and precipitation follow the long term insolation changes in each hemisphere  
 269 during summer until about 2000 years BP to 1500 years BP (Fig. 6). Then trace gases and insolation forcing  
 270 become equivalent in magnitude and small compared to MH insolation forcing, until the last period where trace  
 271 gases lead to a rapid warming. The NH summer cooling reaches about 0.8 °C and is achieved in 4000 years. The  
 272 last 100 year warming reaches 0.6 °C and almost counteracts, for this hemisphere and season, the insolation  
 273 cooling. SH summer (JJAS) and NH Winter (NDJF) temperatures are both characterized by a first 2000 years  
 274 warming. It reaches about 0.4° C. It is followed by a plateau of about 3000 years before the last rapid increase of  
 275 about 0.6° C that reinforces the effect of the Holocene insolation forcing. During SH winter temperature does not  
 276 seem to be driven by the insolation forcing (Fig. 6d). In both hemispheres summer precipitation trends correlate  
 277 well to temperature trends, as it is expected from a hemispheric first order response driven by Clausius  
 278 Clapeyron relationship (Held and Soden, 2006). This is not the case for winter conditions because one needs to  
 279 take into account the changes in the large scale circulation that redistribute heat and energy between regions and  
 280 hemispheres (Braconnot et al., 1997; Saint-Lu et al., 2016).

281 We further estimate the linkages between the long term climate response and the insolation forcing for  
 282 the different latitudinal bands by projecting the zonal mean temperature and precipitation seasonal evolution on  
 283 the seasonal evolution of insolation. We define the seasonal amplitude for each year as the difference between  
 284 the maximum and minimum monthly values. We consider for each latitude the unit vector  $\mathbf{S}$ :

$$285 \mathbf{S} = \frac{\mathbf{SW}_{is-TOA}}{\|\mathbf{SW}_{is-TOA}\|} \quad (1),$$

286 where  $\|\mathbf{SW}_{is-TOA}\|$  represents the norm of the seasonal magnitude of the incoming solar radiation at TOA over  
 287 all time steps ( $\mathbf{SW}_{is-TOA}(t)$ ,  $t=-6000$  years to 0, with an annual time step). Any climatic variable ( $\mathbf{V}$ ) can then be  
 expressed as:

$$288 \mathbf{V}(t) = \alpha(t)\mathbf{S} + \beta(t)\mathbf{b} \quad (2),$$

with:

$$289 \alpha = \mathbf{V} \cdot \mathbf{S} \quad (3),$$

290 and  $\mathbf{b}$  is the unit vector orthogonal to  $\mathbf{S}$ . The ratio  $\alpha/(\alpha + \beta)^{\frac{1}{2}}$  measure in which proportion a signal projects on  
 291 the insolation (Fig. 7). Fig. 7 confirms that the projection of temperature and precipitation on the insolation curve  
 292 is larger in the northern than in the southern hemisphere. The best match is obtained between 10° N and 40° N  
 293 where about 80 % of the temperature signal is a direct response to the insolation forcing. The projections are  
 294 only 50 % in the tropics in the southern hemisphere. These numbers go up to 90 % if a 100 year smoothing is  
 295 applied to temperature. The seasonality precipitations project also to 90 % when considering the filtered signal,  
 296 confirming the strong linkages between temperature and precipitation in the NH over the long time scale. The  
 297 projection is poorer, but not null, when the raw precipitation signal is considered. At the equator and in high  
 298 latitudes in both hemispheres the projection is poor or null. At the equator, the MH insolation forcing favours a  
 299 larger north/south seasonal march of the ITCZ over the ocean and the inland penetration of Afro-Asian monsoon  
 300 precipitation during boreal summer. Surface temperature is reduced in regions where precipitation is enhanced  
 301 due to the combination of increased cloud cover and increased surface evaporation (Braconnot et al., 2007a;  
 302 Joussaume et al., 1999). When monsoon retreats to its modern position, surface temperature in these regions  
 increases, thereby enhancing its seasonal cycle. It is thus out of phase compared to the insolation forcing. This is

303 also true over SH continents where temperatures in regions affected by monsoons do not follow the local  
304 insolation and has similar seasonal evolution than the northern hemisphere. This out of phase relationship is  
305 consistent with glaciers reconstructions (Jomelli et al., 2011). In higher latitude the projection of the raw signal  
306 does not project well because of the large decadal variability. North of 40° N the mixed layer depth is also larger  
307 (about 200 m) than in the tropics (about 70 m), which contribute to damp the seasonal change over the ocean.  
308 Thereby the seasonal temperature response is flatter than the shape of the seasonal insolation forcing, which lead  
309 to a poor projection over mid and high latitudes ocean especially in the ocean dominated SH (Fig. 7). Sea ice  
310 cover has also little change north of 80° N which also damps the changes in seasonality (Fig. 8). These changes  
311 are however amplified by the increase of sea ice during summer in the Arctic resulting from cooler conditions  
312 with time, and by the reduction of the winter sea-ice cover in the Labrador and the Greenland-Iceland-Nordic  
313 seas (Fig. 8a and b). For the snow cover the conditions are contrasted depending on the regions (Fig. 8 b and d),  
314 with an increase decrease of the maximum cover over Eurasia related to long term rise of minimum temperature  
315 (Fig. 8d)

### 316 **3.3 Long term vegetation trends**

317 These long term climate evolutions have a counterpart on the long term evolution of vegetation (Fig. 9).  
318 At the global and hemispheric scale, the long term vegetation trends correspond to reductions or increases of the  
319 area covered by vegetation reaching 2 to 4 % of the total land area depending on vegetation type (Fig. 9). The  
320 global vegetation averages reflect the northern hemisphere changes where most of the vegetated continental  
321 masses are located. As expected from the different long term trend in insolation, the long term evolution of tree  
322 and grass covers are opposite between the two hemispheres. Note however that bare soil slightly increases in  
323 both hemispheres.

324 In the northern hemisphere the changes follow the changes in summer temperature, with the best match  
325 obtained for grass which increases almost linearly until 2000 years BP and then remains quite stable. In the  
326 southern hemisphere the phasing between vegetation change and temperature is not as good, again because this  
327 hemisphere is dominated by ocean conditions rather than land conditions. However, the tree expansion reaches a  
328 maximum between 2000 years BP and 1000 years BP and then the tree cover slightly decreases, which  
329 corresponds to the slight cooling in SH summer temperature. The gross primary productivity (GPP, Fig. 9d) is  
330 driven in both hemispheres by the changes in tree cover. It accounts for a reduction of about 5 PgCy<sup>-1</sup>. It is  
331 however possible that the GPP change is misestimated in this simulation because CO<sub>2</sub> is prescribed in the  
332 atmosphere, which implies that the carbon cycle is not fully interactive. Figure 10 compares the vegetation map  
333 obtained for the pre-industrial period in TRHOLV (50 years around 1850 CE, which corresponds to 150 - 100  
334 years BP) with MH vegetation. It shows that bare soil increases in semi-arid regions in Africa and Asia, as well  
335 as in South Africa and Australia. The reduction in tree PFTs is maximum north of 60° N, in South and Southeast  
336 Asia, Sahel and most of North America. They are replaced by grass PFTs. In the southern hemisphere forest  
337 cover increases in South Africa, South East South America and part of Australia.

338 In the last 100 years the effect of trace gases and in particular the rapid increase of the atmospheric CO<sub>2</sub>  
339 concentration leads to a rapid vegetation change characterized by tree regrowth, which is dominant in the NH  
340 (Figs. 9 and 10). This tree recovery counteracts the reduction from mid Holocene in mid and high NH latitudes  
341 (Fig. 10 b, e, and h). This effect is consistent with the observed historical growth in gross primary production

342 discussed by Campbell et al. (2017). The GPP increase in the last 100 years results from increased atmospheric  
343 CO<sub>2</sub>. It suggests that the CO<sub>2</sub> effect counteracts the tree decline induced by insolation. When reaching 0k BP  
344 (1950 CE), bare soil remains close to PI, grass reduces by 3 % and tree increases by about 3 %.

### 345 **3.4 Regional trends**

346 Figure 11 highlights the long term vegetation trends for three regions that respectively represent climate  
347 conditions north of 60° N, over the Eurasian continent, and in the West African monsoon Sahel/Sahara region.  
348 These are regions for which there are large differences in MH – PI climate and vegetation cover (Figs. 9 and 10).  
349 They have also been chosen because they are widely discussed in the literature and are also considered as tipping  
350 points for future climate change (Lenton et al., 2008). They are well suited to provide an idea of different  
351 characteristics between regions.

352 North of 60° N a substantial reduction of tree at the expense of grass starts at 5000 years BP (Fig. 11 a  
353 and b). Vegetation has almost its pre-industrial conditions around 2500 years BP. The largest trends are found  
354 between 5000 years BP and 2500 years BP in this region and this reflects well the timing of the NH hemisphere  
355 summer cooling. The change in total forest in Eurasia is small. A first change is followed by a second one  
356 around 3000 years BP. Despite the 100 years smoothing applied to all the curves, they exhibit large decadal to  
357 multi centennial variability. Over West Africa (Fig. 11 c), the largest trends start slightly later (4500-5000 years  
358 BP) and are more gradual until 500 years BP. The vegetation trends are also punctuated by several centennial  
359 events that do not alter much the long term evolution as some of these events do in the other two boxes.

360 The variability found for vegetation is also found in temperature and precipitation at the hemispheric  
361 scale (Fig. 6). It is even higher at the regional scale in mid and high latitudes (Fig. 8). This variability is not  
362 present in the imposed forcing. It results from internal noise. Because of this it is difficult for example to say if  
363 the NH hemisphere winter temperature trend was rapid until 4000 years BP and then temperature remains stable,  
364 or if the event impacting temperature and precipitation around 4800 to 4500 years BP masks a more gradual  
365 increase until 3000 years BP as it is the case for NH Summer where the magnitude of the temperature trend is  
366 larger than variability (Fig. 6). Note that some of these internal fluctuations reach half of the total amplitude of  
367 the regional vegetation trends (Fig. 11), and that it is a dominant signal over Eurasia, where the long term mean  
368 change in the total tree cover is small (Fig. 10 and 11). Temperature and precipitation are well correlated at this  
369 centennial time scale (Fig. 6).

370 Despite the dry bias over the Sahel region in this version of the model, the timing of the vegetation  
371 changes over West Africa reported in figure 11 is consistent with the major features discussed for the end of the  
372 African humid period (Hély and Lézine, 2014; Liu et al., 2007). In particular, the replacement of grass by bare  
373 soil starts earlier than the reduction of the tree cover located further south (Fig. 11). At the scale of the Sahel  
374 region, we do not have abrupt but gradual changes in vegetation. It is however abrupt at the grid cell level. These  
375 changes are associated with the long term decline of precipitation, as well as the southward shift of the tropical  
376 rain belt associated with the African monsoon (Fig. 12). The location (latitude) of the rain belt is estimated here  
377 as the location of the maximum summer precipitation zonally averaged between 10 °W and 20 °E over West  
378 Africa. Most of the southward shift of the rain belt occurs between MH and 3500 years BP and correspond to a  
379 difference of about 1.8° N of latitude over this period. Then the southward shift is smaller, with a total shift of  
380 2.5° N of latitude diagnosed in this simulation. The comparison of Figs. 11 and 12 clearly shows that the rapid

381 decrease of vegetation occurs after the rapid southward shift of the rain belt. An interesting point is that the  
382 amount of precipitation is also shifted in time compared to the location of the rain belt. It suggests that the  
383 vegetation feedback on precipitation is still effective during the first period of precipitation decline and that it  
384 might have amplify the reduction of precipitation when vegetation is reduced over the Sahel region.

385 As seen in Fig. 10, the NH decrease in forest cover is mainly driven by the changes that occur north of  
386 60°N (Figs. 8 and 10). These trends reflect more or less what is expected from observations (Bigelow et al.,  
387 2003; Jansen et al., 2007; Wanner et al., 2008). It results from the summer cooling that affects both the summer  
388 sea-ice cover in the Artic, the summer snow cover over the adjacent continent and the amplification of the  
389 insolation forcing south of 70° N by snow/vegetation albedo feedback. Further south over Eurasia, Fig. 11  
390 suggests that there are only marginal changes in Eurasia in terms of vegetation. Fig. 13 shows the total tree cover  
391 over this region does not reflect well the mosaic vegetation and forest composition. Indeed, the long term  
392 decrease in forest is dominated by the decrease in temperate and boreal deciduous trees. Boreal needle leaf  
393 evergreen trees do not change whereas the temperate ones increase. This figure also highlights that the long term  
394 change in Eurasian tree composition throughout the mid to late Holocene is punctuated by centennial variability.  
395 The different trees have also different timing and variability. Boreal forests are more sensitive to variability  
396 during the first 3000 years of the simulation, whereas, temperate broadleaf tree exhibit larger variability in the  
397 second half. The large events have a climatic counterpart (Fig. 8), so that the composition of the vegetation is a  
398 result of a combined response to the long term climatic change and to variability. These two effects can lead to  
399 different vegetation composition depending on stable or unstable vegetation states (Scheffer et al., 2012).  
400 Decadal vegetation changes have been discussed for recent climate in these regions (Abis and Brovkin, 2017),  
401 which suggests that despite the fact that our dynamical vegetation model might underestimate vegetation  
402 resilience, the rapid changes in vegetation mosaic is a key signal over Eurasia. Future model data comparisons  
403 should consider composition changes and variability to properly discuss vegetation changes over this region.

## 404 **4 Vegetation, uncertainties and multiple vegetation states**

### 405 **4.1 Simulated versus reconstructed vegetation**

406 Section 3 shows how climate and vegetation respond to insolation and trace gases. The simulated  
407 changes are in broad agreement with what is expected from various sources of data. However, section 2  
408 mentions model adjustments and biases. They all contribute to the difficulty to produce the right vegetation  
409 changes at the right place, at the right time and for the right reasons. It is thus important to fully understand what  
410 we can expect in terms of realism from this simulation. We investigate it for the mid-Holocene and modern  
411 climate for which we can use the BIOME6000 vegetation reconstruction (Harrison, 2017).

412 The dynamical vegetation module simulates fractional cover of 13 PFTs. These PFTs cannot be directly  
413 compared with the reconstructed biome types based on pollen and plant macrofossil data from the BIOME 6000  
414 dataset (Harrison, 2017). In order to facilitate the comparison, we converted the simulated PFTs into eight mega-  
415 biomes, using the biomization method algorithm proposed by Prentice et al. (2011). The algorithm uses a  
416 mixture of simulated climate and vegetation characteristics (see appendix and Fig. A2). Alternative thresholds as  
417 proposed in previous studies (Joos et al., 2004; Prentice et al., 2011) were tested to account for the uncertainties  
418 in the biomization method (see Fig. A2). At first look MH-Vnone reproduces the large scale pattern found in the

419 BIOME6000 reconstruction (Fig. 14a). The comparison however indicates that the boreal forest tree line is  
420 located too far south. It results from a combination of a cold bias in temperature in these regions and a systematic  
421 underestimation of forest biomass in Siberia with ORCHIDEE when forced by observed present-day climate  
422 (Guimberteau et al., 2018). Such underestimation of tree biomass could lead to too low tree height in  
423 ORCHIDEE, and thus to the replacement of boreal forest by dry woodland according to the biomization  
424 algorithm (Fig. A2a). Also, vegetation is underestimated in West Africa, consistent with a dry bias (not shown).  
425 The underestimation of the African monsoon precipitation is present in several simulations with the IPSL model  
426 (Braconnot and Kageyama, 2015), and is slightly enhanced in summer when the dynamical vegetation is active.  
427 With interactive vegetation however equatorial Africa is more humid (Fig. 15a). Fig. 14c provides an idea of the  
428 major mismatches between simulated vegetation and the BIOME6000 reconstructions. In particular the  
429 simulation produces too much desert where we should find grass and shrub. It also produces too much tundra  
430 instead of boreal forest, and too much savanah and dry woodland in several places that should be covered by  
431 temperate-tree, boreal-tree or tundra, confirming the visual map comparison (Fig. 14c). Similar results are found  
432 when considering the pre-industrial climate in TRHOLV compared to the BIOME6000 pre-industrial biome  
433 reconstruction (Fig. A2d). These are systematic biases. These systematic biases are confirmed when comparing  
434 the simulated PFTs for PI with those of the 1860 CE map estimated from observations and used in simulations  
435 with prescribed vegetation (see Tab. A2 for regions without land use).

436 It is not possible to estimate the vegetation feedback on the long term climate evolution from the  
437 transient simulation. It is however possible to infer how the dynamical vegetation affects the mean climatology  
438 for the MH, period for which simulations with prescribed and dynamic vegetation are available. Metrics  
439 discussed in section 2.4 (Fig. 3) show that the introduction of the dynamical vegetation in the model reduces the  
440 amount of precipitation and that the climate is dryer. The simulations with dynamical vegetation only consider  
441 natural vegetation, whereas the 1860 CE map we prescribe when vegetation is fixed include land use. In regions  
442 affected by land use all MH simulations produce less bare soil (3 %), more tropical trees (5 %), similar temperate  
443 tree cover, increased boreal tree cover (10 %) and a different distribution between C3 versus C4 grass (see Tab.  
444 A2). In Eurasia where croplands are replaced by forest, the lower forest albedo induces warmer surface  
445 conditions (Fig. 15b). Also, when snow combines with forest instead of grasses, the snow/vegetation albedo is  
446 lower leading to the positive snow-forest feedback widely discussed for the last glacial inception (de Noblet et  
447 al., 1996; Kutzbach et al., 1996). Fig. 15a also highlights that precipitation is increased over the African tropical  
448 forest and reduced over South America. In most regions the impact of vegetation is much smaller than the impact  
449 of the changes in the land surface hydrology and forcing strategy discussed in sections 2.3 (Fig. 2).

450 The differences between the MH simulated vegetation map and the 1860 CE map reflect both  
451 systematic model biases and vegetation changes related to the MH climate differences with PI. We can infer  
452 from Figs.15 and 16 that vegetation has a positive warming feedback in the high latitudes during MH. Part of the  
453 differences between the MH and the PI conditions in Fig. 15c and d are dominated by the impact of vegetation.  
454 Similar patterns as those obtained for the impact of vegetation are found over Eurasia for temperature, or south  
455 East Asia and North America for precipitation. For the grid points where BIOME6000 data are available for both  
456 MH and PI (0k), the major simulated biome changes occur for Savana&Wood and Grass&Shrub (Fig. 14e).  
457 Differences are also found for tree and tundra, to a lesser extent. The comparison with similar estimates from  
458 BIOME6000 reconstructions indicates that Grass&Shrub exhibit the major changes and that tree show larger

459 differences compared to the simulation. The model shift between Savana&Wood and Grass&Shrub is consistent  
460 with the noted bias for Savana and the fact that the tree cover is underestimated in norther NH latitudes (Fig. 14).

461 Note that the vegetation differences found between the historical period and the PI period in TRHOLV  
462 are not negligible. We can estimate from Figs. 15a and b that neglecting land use leads to an underestimation of  
463 about 1° C in Eurasia between the MH and PI in this TRHOLV simulation. Depending if PI or the historical  
464 period is used as reference the magnitude of the MH changes in vegetation and climate would be different. Also  
465 land use has regional impacts and should be considered in PI or in the historical period. This stresses that  
466 quantitative model-data comparison should be considered with care, knowing that both the reference period (PI  
467 or historical) and the complexity of the land surface model (prescribed vegetation, natural dynamical vegetation,  
468 land use...) can easily lead to 1 °C difference in some regions.

469

## 470 **4.2 Multiple vegetation states for the pre-industrial climate**

471 Another source of uncertainty concerns the stability of the simulated vegetation maps. Several studies  
472 suggest that the initial state has only minor impact on the final climate because there is almost no changes in the  
473 thermohaline circulation over this period and models do not exhibit major climate bifurcations (e.g. Bathiany et  
474 al., 2012). This is the main argument used by Singarayer et al. (2010) to justify that their suite of snap shot  
475 experiments may provide reasonable transient climate vision when put together. Is it the case in the TRHOLV  
476 simulation when vegetation is fully interactive? This transient simulation does not exhibit much change in  
477 indices of thermohaline circulation that remains close to 16-18 Sv ( $1 \text{ Sv} = 10^6 \text{m}^3 \cdot \text{s}^{-1}$ ) throughout the period. The  
478 global metrics (Fig. 3) show that at the global scale the results of the TRHOLV simulations for PI (around 100  
479 BP = 1860 CE) are similar to those of PI-Vnone. It is also the case for seasonal and extratropical/tropical values  
480 (Fig. A1). We can therefore conclude that there is no difference in mean surface climate characteristics between  
481 the snap shot PI-Vnone experiments and the PI period simulated in transient TRHOLV simulation.

482 Then, is the vegetation also similar to the one simulated in PI-VNNone? The PI vegetation simulated in  
483 TRHOLV shows little differences to the one found for PI-Vnone (Fig. 10 c, f, and i). The relative percentages of  
484 land covered by the different vegetation classes correspond to 15 % for bare soil, 41 % for grass and 43 % for  
485 tree respectively. These values are similar to the one found for PI-VNNone (15 %, 40 % and 44 % respectively)  
486 within 1 % error bar. This doesn't necessarily hold at the regional scale where regional differences are also found  
487 between PI-THROLV and PI-Vnone. Indeed, Fig. 10 indicates differences in tree and grass cover in Eurasia  
488 around 60° N and different geographical coverage between bare soil, grass and trees over South Africa and  
489 Australia. These differences are very small compared to the differences between MH and PI in TRHOLV, but  
490 are as large as the difference between hist and PI in a few places in Eurasia. As seen in previous section, these  
491 are regions where variability is large and vegetation instable.

492 We also tested if the PI vegetation and climate would also be similar when starting from MH-Vmap  
493 instead of MH-Vnone (dark pink and orange lines in Fig. 4d, e and f). This is also a way to have a better idea of  
494 the range of response one would expect from ensemble simulations, knowing that we only ran one full transient  
495 simulation. For the PI-Vmap simulation, the orbital parameters and trace gases were first prescribed to pre-  
496 industrial conditions for 15 years while maintaining the vegetation PFTs in each grid cell to those obtained in  
497 MH-Vmap (Tab. 2, Fig. 4). Then, the dynamical vegetation was switched on. It induces a rapid transition of the

498 major PFTs that takes about 10 years before a new global equilibrium is reached (Fig. 4 d, e and f). For PI-  
499 VNone presented in section 2.4 the same procedure was applied, but the dynamical vegetation was switched on  
500 after 5 years (Tab. 2 and Fig. 4), and the new equilibrium state is reached without any relaxation or rapid  
501 transition.

502 PI-Vnone and PI-Vmap converge to different global vegetation states (Fig. 4). Compared to the values  
503 listed above for PI-Vnone and PI-TRHOLV the respective covers of bare soil, grass and tree for PI-Vmap are  
504 20 %, 37 % and 43 %. In particular PI-Vmap produces a larger bare soil cover than PI-Vnone (Fig. 4d). It is even  
505 larger than the total bare soil cover found in the 1860 CE map used in PI simulations when vegetation is  
506 prescribed (Fig. 4). Interestingly part of these differences between Vmap and Vnone, are found in the southern  
507 hemisphere and the northern edge of the African and Indian monsoon regions. Since there is almost no  
508 difference in MH vegetation between Vmap and Vnone, these differences in PI vegetation drive the vegetation  
509 differences between MH and PI (Fig. 16). The MH simulated changes seem larger with Vmap. Previous  
510 assessment of model results against vegetation and paleoclimate reconstructions (e.g. Harrison et al., 2014;  
511 Harrison et al., 1998) suggest that MH – PI vegetation for Vmap would look in better agreement with  
512 reconstructed changes from observations in terms of forest expansion in the northern hemisphere or grasses in  
513 Sahel (Fig. 16). However, the modern vegetation map for this PI-Vmap simulation has even less forest than PI-  
514 Vnone north of 55° N (Fig. 4 e, f and i), for which forest is already underestimated (Fig. A2). These differences  
515 in PI vegetation have only a small counterpart in climate. It corresponds to cooler condition in the mid and high  
516 norther latitude (Fig. 15). In annual mean there is almost no impact on precipitation (Fig. 15). In terms of climate  
517 these two simulations are very similar, and closer to each other than to other simulations, whatever the season or  
518 the latitudinal band (Fig. A1). The small differences in climate listed above are thus too small to be captured by  
519 global metrics. It suggests that there is no direct relationship between the different vegetation maps and model  
520 performances. The different vegetation maps are obtained with a similar climate, which indicates that in this  
521 model multiple global and vegetation states are possible under pre-industrial climate or that tiny climate  
522 differences can lead to different vegetation.

## 523 **5 Conclusion**

524 This long transient simulation over the last 6000 years with the IPSL climate model is one of the first  
525 simulations over this period with a general circulation model including a full interactive carbon cycle and  
526 dynamical vegetation. Several adjustments were made to set up the model version and the transient simulations.  
527 Most of them have a larger impact on the model climatology than the dynamical vegetation feedback, and  
528 remind us that fast feedbacks occur in coupled systems so that any evaluation of surface flux should consider  
529 both the flux itself and the climate or atmospheric variables used to compute it (Torres et al., 2018). We show  
530 that, despite some model biases that are amplified by the additional degree of freedom resulting from the  
531 coupling between vegetation and climate, the model reproduces reasonably well the large scale features in  
532 climate and vegetation changes expected from reconstructions over this period. The transient simulation exhibit  
533 little change in annual mean climate throughout the last 6000 years (not shown). The seasonal cycle is the main  
534 driver of the climate and vegetation changes, except in the last part of the simulation when the rapid greenhouse  
535 gas concentration increase leads to a rapid global warming. There has been lots of discussion on the sign of the  
536 trends in the northern mid-latitude following the results of the first coupled ocean-atmosphere simulation with

537 the CCSM3 model across the deglaciation (Liu et al., 2014). Our results seem in broad agreement with the 6000  
538 to 0 years BP part of the revised estimates by Marsicek et al. (2018).

539 The analysis of vegetation differences between PI-Vmap and PI-VNone raises once more the possibility  
540 for multiple vegetation equilibrium under pre-industrial or modern conditions as it has been widely discussed  
541 previously (e.g. Brovkin et al., 2002; Claussen, 2009). Here we have both global and regional differences. Our  
542 results are however puzzling, because we only find limited differences between the PI-Vnone snapshot  
543 simulation and the PI climate and vegetation produced at the end of TRHOLV. These simulations start from the  
544 same initial state and in one case PI condition are switch on in the forcing, whereas the other case the 6000 years  
545 long term forcing in insolation and trace gases is applied to the model. An ensemble of simulations would be  
546 needed to fully assess vegetation stability. In the northern hemisphere and over forest areas, MH-Vmap produced  
547 slightly less trees than MH-Vnone. It might have been amplified by snow albedo feedback under the PI  
548 conditions that are characterized by a colder than MH climate in high latitudes in response to reduced incoming  
549 solar radiation associated with lower obliquity. The differences between the southern and northern hemispheres  
550 characterized by large differences in grasses and bare soil are more difficult to understand and suggest different  
551 response to the changes in southern hemisphere seasonality. This is in favor of a different equilibrium that is  
552 only partially induced by climate-vegetation feedback. We need also to raise the point that there is still a very  
553 small probability that these differences come from inconsistent modeling when vegetation is prescribed or when  
554 we use the dynamical model. This should not be the case because it would not explain why vegetation is  
555 sensitive to initial state in PI and not in MH. It is also possible that the climate instability induced by the change  
556 from one year to the other in insolation and trace gases leads to rapid amplification of climate in high latitude,  
557 which is more effective under the cooling high latitude condition found in PI. The strongest conclusion from  
558 these simulations is that the vegetation-climate system is more sensitive under the pre-industrial conditions (at  
559 least in the northern hemisphere).

560 Our analyses show that the MH-PI changes in climate and vegetation is similar between snapshot  
561 experiments and in the long transient simulation. What is the value added then of the transient simulation? The  
562 good point is that model evaluation can be done on snapshot experiments, which fully validate the view that the  
563 mid-Holocene is a good period for model benchmarking in the Paleoclimate Modeling Intercomparison Project  
564 (Kageyama et al., 2018). However the MH – PI climate conditions mask the long term history and the relative  
565 timing and the rate of the changes. The major changes occur between 5000 and 2000 years BP and the exact  
566 timing depends on regions. In our simulation the forest reduction in the northern hemisphere starts earlier than  
567 the vegetation changes in Africa. It also ends earlier. The last period reflects the increase in trace gases with a  
568 rapid regrowth of tree in the last 100 years when CO<sub>2</sub> and temperature increase at a rate not seen over the last  
569 6000 to 2000 years. Some of these results already appear in previous simulations with intermediate complexity  
570 models (Crucifix et al., 2002; Renssen et al., 2012). Using the more sophisticated model with a representation of  
571 different types of tree brings new results. Even though the total forest cover does not vary much throughout the  
572 Holocene in TRHOLV, the composition of the forest varies more substantially, with different relative timing  
573 between the different PFTs.

574 We mainly consider here surface variables that have a rapid adjustment with the external forcing. Also,  
575 we only consider long term trends in this study, but the results highlight that centennial variability plays an  
576 important role to shape the response of climate and vegetation to the Holocene external forcing at regional scale.

577 In depth analyses of ice covered regions and of the ocean response would be needed to tell whether the  
 578 characteristics of variability depends or not on the pace of climate change. It would guide the development of  
 579 methodologies to assess the vegetation instabilities as the one seen in Eurasia. They might share some  
 580 similarities with the vegetation variability reported in this region for the recent period (Abis and Brovkin, 2017).  
 581 These simulations offers the possibility to analyze the simulated internal instability of vegetation that could be  
 582 partly driven by climate noise (Alexandrov et al., 2018). The different time scales involved in this long term  
 583 evolution can be seen as an interesting laboratory for further investigation in this respect.

584 These results allow us to answer the four questions raised in the introduction: 1. Insolation is the main  
 585 driver of the climate and vegetation in the NH and in the SH for summer and the response to the insolation  
 586 forcing in north of 80° N and in the SH is muted by ocean or sea-ice and snow feedback; 2. The impact of the  
 587 trace gases is effective in the last 100 years of the simulation and counteracts the effect of the Holocene  
 588 insolation on both climate and vegetation in the NH and enhanced it in the SH; 3. The timing of the vegetation  
 589 changes depends on region with tree regression starting first in high NH latitudes; 4. Centennial variability is  
 590 large and need to be accounted for to understand regional changes, in particular over Eurasia. It has implication  
 591 for model data comparison. High resolution records from tree rings, speleothems or varved sediments are unique  
 592 records to assess climate variability, but they are sparse and most of them span non continuous periods of time.  
 593 The model framework, even though it is an imperfect representation of reality, offers a consistent framework to  
 594 discuss the consistency between records. To go further in this direction, specific methodology needs to be  
 595 designed to assess the climate-vegetation dynamics over a long time scale without putting too much weight on  
 596 inherent model biases. Another difficulty to properly assess these model results against paleoclimate  
 597 reconstructions is related to the fact that we only represent natural vegetation, and neglect land use and also  
 598 aerosols other than dust and sea-salt. Therefore the PI and historical climate cannot be realistically reproduced,  
 599 even though most of the characteristics we report are compatible with what has been observed. In addition, the  
 600 magnitude of the simulated differences between MH and modern conditions depends on the reference period.  
 601 This opens new challenges for model-data comparisons to properly analyze the pace of changes and climate  
 602 variability. It suggests that more needs to be done to derive criteria allowing us to assess the processes leading to  
 603 the observed changes rather than the changes themselves.

## 604 **6 Appendix**

### 605 **6.1 A1 Spatio-temporal agreement between model results and observations in the extratropics and** 606 **tropics**

607 Figure 3 highlights the model-observation agreement for the pre-industrial climate considering global  
 608 metrics, commonly used to evaluate model climatology. The mean bias ( $Bias_{xy}$ ) represents the difference  
 609 between the spatio-temporal averages of a simulated variable with observations. Here all metrics consider fifty  
 610 year averages from observations or reanalysis products. We estimate the spatio-temporal mean of each variable  
 611 as:

$$Var_{xy} = \frac{1}{T} \sum_{i,j,t} w_{i,j} Var_{i,j,t} \quad (4)$$

612 Where  $w_{i,j}$  (with  $\sum_{i,j} w_{i,j} = 1$ ) represents the ratio of the surface of the grid-cell to the total surface of  
 613 the grid, and  $T$  the number of time steps. If we call  $Var_{mod}$  the simulated variable and  $Var_{obs}$  the observed  
 614 one, the mean bias expressed as

$$Bias_{xy} = Var_{mod_{xy}} - Var_{obs_{xy}} \quad (5)$$

615 measures the mean difference over the whole spatial domain and all time steps (12 climatological months).

616 The RMSE ( $rms_{xyt}$ ) is the Root Mean Squared Error computed between the model and the  
 617 reference over the twelve climatological months:

$$rms_{xyt} = \sqrt{\frac{1}{T} \sum_{i,j,t} w_{i,j} (Var_{mod_{i,j,t}} - Var_{obs_{i,j,t}})^2} \quad (6)$$

618 The metric is sensitive to the value of the mean bias, and provides a measure of the spatio-temporal  
 619 agreement between the model and the reference.

620 We present the global metrics only in the main text (Fig. 3). We complete the analyses by computing  
 621 the same metrics (bias and root mean square) at the seasonal time scale and for 3 latitudinal bands. We restrict  
 622 the figure to surface air temperature and precipitation that reflects well the major differences. It shows that these  
 623 measures capture differences between the IPSLCM5A-LR version of the IPSL model (Dufresne et al., 2013) and  
 624 the new version developed for the TRHOLV transient simulation (see section 2). It also highlights the impact of  
 625 running the model with the dynamical vegetation. However, as in Fig. 3 the simulations with different MH  
 626 conditions for the interactive vegetation, as well as the PI conditions obtained after 5900 years of transient  
 627 simulation are difficult to distinguish. Differences become significant again when considering the last 50 years  
 628 of the transient simulations that are affected by increase greenhouse gases.

## 629 **6.2 A2 Biomization and sensitivity analysis.**

630 Table A2 show the different ORCHIDEE PFT for the different MH and PI simulations, considering the  
 631 regions that are affected, or regions that are not affected by land use in the pre-industrial simulation with  
 632 vegetation prescribed to the 1860 observed values.

633 To convert the ORCHIDEE model PFTs into mega biomes we use the algorithm proposed by Prentice  
 634 et al. (2011) and used by Zhu et al. (2018). Fig. A2a shows the different thresholds used in the algorithm. The  
 635 black numbers correspond to the default values used to produce Fig. 14 in the main text. Since some of these  
 636 thresholds are somehow artificially defined, we also tested the robustness of our comparison by running  
 637 sensitivity tests. These tests considered successively different threshold in Growing Degree Days above 5 °C  
 638 (GDD5), canopy height and foliage projective cover as indicated in red on Fig. A2a.

639 The different thresholds induce only slight difference on the biome map for a given simulation. The  
 640 largest sensitivity is obtained for the height. When 10 m is used instead of 6 m, a larger cover of savannah and  
 641 dry woodland is estimated from the simulations in mid and high northern latitudes. In these latitudes also, a  
 642 large sensitivity is found when the GDD5 limit is set to 500 °C d<sup>-1</sup> instead of 350 °C d<sup>-1</sup> between tundra and  
 643 savannah and dry woodland or boreal forest.

644 The same analyses transformation into megabiomes was performed for the Vmap and Vnone  
 645 simulations. Similar sensitivity is found to the different thresholds for these two simulations (Fig. A2b). The  
 646 synthesis of the goodness of fit between model and data is presented in Fig. A2c. It shows that the two

647 simulations provide as expected very similar results when compared to the MH BIOME6000 map. It is  
648 interesting to note that the different thresholds do not have a large impact on the model data comparison, when  
649 all data points are considered. The change in GDD5 limit produces tundra in better agreement with pollen data,  
650 and the canopy height better results with savannah and dry woodland. Note however that this result is in part due  
651 to the fact that there is little data in regions where the impact is the largest (Fig. 6 in the main text).

652 The same procedure was also applied to the PI Vnone and PI-Vmap simulations. The overall  
653 correctness (percentage of reconstruction sites showing the same megabiome between model and data) is similar  
654 as the one obtained for MH (37 % for MH and 35 % for PI). These numbers are close to the percentages derived  
655 by Dallmeyer et al. (2019) using a climate-based biomization method (i.e. use ESM modeled climate states to  
656 force a biogeography model to simulate the biome distribution), which gives 33 % and 39 % with two IPSL  
657 model versions for pre-industrial

658 *Acknowledgments.* We would like to thanks our colleagues from the IPSL global climate model group  
659 for their help in setting up this intermediate version of the IPSL model. In particular the ORCHIDEE group  
660 provided good advices for the closure of the hydrological cycle in the land surface scheme (Philippe Peylin,  
661 Agnès Ducharne, Frédéric Cheruy and Joséfine Gattas) or the snow ablation (Sylvie Charbit and Christophe  
662 Dumas). The workflow for these long simulations benefits from the development of Anne Cozic and Arnaud  
663 Caubel. Discussions with Philippe Ciais and Yves Balkansky were also at the origin of the choice of the land  
664 surface model complexity and aerosols forcing strategy. We are grateful to the anonymous reviewers for their  
665 constructive comments that helped to improve the manuscript. We acknowledge PRACE for awarding us access  
666 to Curie at GENCI@CEA, France (THROL project) to start the simulations. The simulations were also  
667 performed using HPC resources from GENCI-TGCC thanks to a high end computing access grant and to our  
668 annual allocation time (gen2212). This work is supported by the JPI-Belmont PACMEDY project (N ° ANR-15-  
669 **JCLI-0003-01**).

670

Simulation	Comment	Initial state	Forcing
<b>Reference MH) simulations with prescribed vegetation map</b>			
MH_PMIP3	Reference PMIP3-CMIP5 IPSL simulation (Kageyama et al., 2013a)	Previous MH long term simulation with the model used to test model configuration	PMIP3
MH_FPMIP4 (S_Sr04)	Reference version used here, with vegetation prescribed to the 1860 vegetation map as in PMIP3-CMIP5.	From year 250 of MH_L11AerEv below	PMIP4
<b>Reference PI simulations with prescribed vegetation map</b>			
PI_PMIP3	Reference PMIP3-CMIP5 IPSL simulation (Dufresne et al., 2013; Kageyama et al., 2013a)		PMIP3
PI_FPMIP4	As L11AerEv but with pre industrial trace gases and Earth's orbital parameters		PMIP4
<b>MH sensitivity experiments with prescribed vegetation map</b>			
MH_L11 (S_Sr01)	As PMIP3, but with new version of land surface model (hydrology and snow model)	From the last MH test of the new model configuration (new version of ORCHIDEE)	PMIP3
MH_L11Aer (S_Sr02)	As L11, but only dust and sea-salt considered in the aerosol forcing (Aer)	Same as L11	PMIP3
MH_L11AerEv (S_Sr03)	As L11aer, but with factor to limit bare soil evaporation (Ev)	From year 250 of L11Aer	PMIP3

672

673 Table 1. Tests done to set up the model IPSL version in which we included the dynamical vegetation.  
674 For all these simulations the vegetation map is prescribed to the 1860 CE map used in PI-PMIP3. The different  
675 columns highlight the name of the test and the initial state to better isolate the different factors contributing to the  
676 adjustment curves in Fig. 1. We include in parenthesis the tag of the simulation that corresponds to our internal  
677 nomenclature for memory.

678

Simulation	Comment	Initial state	forcing
<b>Reference Mid Holocene (MH) and PI simulations with dynamical vegetation</b>			
MH-Vnone (V-Sr09)	L11AerEv configuration but initial state with bare soil everywhere	Year 250 of L11Aer for atmosphere ocean and sea ice	PMIP3
MH-Vnone_FPMIP4 (V-Sr12)*	Same simulation as MH-Vnone, but using the PMIP4 trace gases forcing	Year250 of MH-Vnone for all model components	PMIP4
PI-Vnone (V_Sr12) *	Preindustrial simulation corresponding to the MH simulations starting from bare soil	Year 500 of MH-Vnone-FPMIP4 for all model components	PMIP4
<b>Reference transient simulation of the last 6000 years with dynamical vegetation</b>			
TRHOLV	Transient mid Holocene to present day simulation with dynamical vegetation	Year 500 of MH-Vnone-FPMIP4 for all model components	PMIP4
<b>Sensitivity experiments with dynamical vegetation</b>			
MH-Vmap (V_Sr10)	As L11AerEv, but vegetation map and soil initial state from an off line ORCHIDEE vegetation map	Year 250 or L11AerEv for atmosphere, ocean and sea-ice	PMIP3
MH-Vmap_FPMIP4 (V_Sr11)	Same simulation as MH-Vmap, but using the PMIP4 trace gases forcing	Year 200 of MH-Vmap, for all model components	PMIP4
PI-Vmap (V_Sr07)	Preindustrial simulation corresponding to the MH simulation starting from the off line ORCHIDEE map	Year 250 of Vmap_FPMIP4, for all model components.	PMIP4

680

681 Table 2. Simulations run to initialize the dynamical vegetation starting from bare soil or from vegetation  
682 map and soil moisture resulting from an off line ORCHIDEE simulation with dynamical vegetation switch on  
683 and using the PI L11 simulated climate as boundary conditions. Simulations with an \* are considered as  
684 references for the model version and the transient simulations. We include in parentheses the tag of the  
685 simulation that corresponds to our internal nomenclature for memory.

686

PFT	Regions with landuse				Regions without landuse							
	MH TRHOLV	MH Vnone	MH Vmap	PI 1860	MH TRHOLV	MH Vnone	MH Vmap	PI TRHOLV	PI Vnone	PI Vmap	PI 1860	Hist TRHOLV
1 - Bare soil	9	9	8	12	21	22	22	24	23	28	26	23
2 - tropical broad-leaved evergreen	15	15	15	13	5	5	5	5	5	5	8	5
3 - tropical broad-leaved raingreen	8	8	8	11	3	3	3	3	3	3	2	3
4 - temperate needleleaf evergreen	8	8	8	5	1	1	1	1	1	1	2	1
5 - temperate broad-leaved evergreen	4	4	4	6	1	0	0	1	1	1	3	1
6 - temperate broad-leaved summergreen	9	8	8	8	2	2	2	2	2	2	2	2
7 - boreal needleleaf evergreen	9	9	9	2	13	13	11	8	10	9	8	11
8 - boreal broad-leaved summergreen	3	3	3	1	4	5	4	3	3	3	8	3
9 - boreal needleleaf summergreen	1	1	1	0	4	4	4	3	3	2	4	3
10 - C3 grass	17	17	16	23	37	36	36	41	41	39	32	38
11 - C4 grass	18	18	20	13	10	10	12	10	9	8	5	10
12 - C3 agriculture	0	0	0	4	0	0	0	0	0	0	0	0
13 - C4 agriculture	0	0	0	2	0	0	0	0	0	0	0	0

687 Table A2. Distribution of ORCHIDEE 13 PFTs (%) in different simulations and the PI 1860 CE map  
688 used as boundary conditions when vegetation is prescribed from pre industrial observations. If the PI 1860 CE  
689 fraction of land use in a grid box is larger than 0.01 then the grid box is considered as covered with land use. The  
690 percentage is computed for each region separately, each region having its own total area. The error bars are  
691 about 0.5, which is accounted for in the table by neglected decimals in the estimates.

692

694 **7 Figure Caption**

695 Figure 1: Illustration of the effect of the different adjustments made to produce mid-Holocene simulations with  
 696 the modified version of the IPSLCM5A-MR model in which the land surface model ORCHIDEE includes a  
 697 different soil hydrology and snow models (see text for details). The three panels show the global average of a)  
 698 net surface heat flux ( $\text{W m}^{-2}$ ), b) evaporation ( $\text{kg m}^{-2}$ ), and c) 2 m air temperature ( $^{\circ}\text{C}$ ). The different color lines  
 699 represent the results for the different simulations reported in Table 1.  
 700

701 Figure 2: Mid Holocene annual mean precipitation ( $\text{mm d}^{-1}$ ) and 2 m air temperature ( $^{\circ}\text{C}$ ) differences between  
 702 a) and b) L11Aer and L11, c) and d) L11 and PMIP3, e) and f) PMIP3L11AerEv and L11Aer, and g) and h) FPMIP4  
 703 and PMIP3. See Table 1 and text for the details about the different simulations.  
 704

705 Figure 3. a) Spatio-temporal root mean square differences ( $\text{rms}_{\text{xyt}}$ ) and b) annual mean global model bias  
 706 ( $\text{bias}_{\text{xy}}$ ) computed on the annual cycle (twelve climatological months) over the globe for the different pre-  
 707 industrial simulations considered in this manuscript (color lines) and individual simulations of the CMIP5 multi-  
 708 model ensemble (grey lines). The metrics for the different variables are presented as parallel coordinates, each  
 709 of them having their own vertical axis with corresponding values. In these plots,  $t_a$  stands for temperature ( $^{\circ}\text{C}$ )  
 710 with  $s$  for surface, 850 and 200 for 850 and 200 hPa respectively,  $pr_w$  for total water content ( $\text{g kg}^{-1}$ ),  $pr$  for  
 711 precipitation ( $\text{mm d}^{-1}$ ),  $rl_{\text{out}}$  for outgoing long wave radiation ( $\text{W m}^{-2}$ ),  $rl_{\text{tcre}}$  and  $rl_{\text{tcre}}$  for the cloud radiative  
 712 effect at the top of the atmosphere in the short wave and long wave radiation respectively ( $\text{W m}^{-2}$ ). See annex  
 713 A1 for details on the metrics.  
 714

715 Figure 4. Long term adjustment of vegetation for a), b), and c) mid Holocene (MH) and c), d) and e)  
 716 preindustrial (PI) climate, when starting from bare soil ( $V_{\text{none}}$ ) or from a vegetation map ( $V_{\text{map}}$ ). The 13  
 717 ORCHIDEE PFTs have been gathered as bare soil, grass, tree and land-use. When the dynamical vegetation is  
 718 active only natural vegetation is considered. Land-use is thus only present in one simulation, corresponding to a  
 719 pre-industrial map used as reference in the IPSL model (Dufresne et al. 2013). The corresponding vegetation is  
 720 referred to as  $PI_{\text{prescribed}}$ . The x axis is in months, starting from 0, which allows to plot all the simulation that  
 721 have their own internal calendar on the same axis.  
 722

723 Figure 5: Evolution of trace gases:  $\text{CO}_2$  (ppm),  $\text{CH}_4$  (ppb) and  $\text{N}_2\text{O}$  (ppb), and seasonal amplitude (maximum  
 724 annual – minimum annual monthly values) of the incoming solar radiation at the top of the atmosphere ( $\text{W m}^{-2}$ )  
 725 averaged over the northern (black line) and the southern (red line) hemispheres. These forcing factors  
 726 correspond to the PMIP4 experimental design discussed by Otto-Bliesner et al. (2017).  
 727

728 Figure 6. Long term evolution of incoming solar radiation at the top of the atmosphere (TOA) ( $\text{W m}^{-2}$ , top panel)  
 729 and associated response of temperature ( $^{\circ}\text{C}$ ) and precipitation ( $\text{mm y}^{-1}$ ) expressed as a difference with the 6000  
 730 years PB initial state and smoothed by a 100 year running mean) for a) NH Summer, b) NH winter, c) SH  
 731 summer, and d) SH winter. Temperatures are plotted in red and precipitation in blue for summer, and they are  
 732 respectively plotted in orange and green for winter. NH Summer and SH Winter correspond to June to  
 733 September averages whereas NH winter and SH summer correspond to December to March averages. All  
 734 curves, except insolation, have been smoothed by a 100 years running mean.  
 735

736 Figure 7: Fraction of the evolution of the seasonal amplitude of temperature (red) and precipitation (blue)  
 737 represented by the projection of these climate variables on the evolution of the seasonal amplitude of  
 738 insolation as a function of latitude. The solid line stands for the raw signal and the dotted line for the signal  
 739 after a 100s year smoothing.  
 740

741 Figure 8: a) total change in snow cover ( $\text{kg m}^{-2}$ ) and sea ice fraction (%) integrated over the last 6000 years, and  
 742 evolution from the Mid Holocene of annual mean maximum summer and minimum winter values for b) sea ice  
 743 averages over the northern hemisphere, c) snow (solid lines) and 2 m air temperature (dotted lines) average for  
 744 all regions north of  $60^{\circ}\text{N}$ , and d) snow and 2m air temperature over Eurasia. In b), c), and d) black, dark blue  
 745 and light blue stand respectively for the annual mean, maximum and minimum annual monthly values for sea-

746 ice or snow cover, and black, green and red for annual mean, annual minimum and annual maximum air  
747 temperature.

748

749 Figure 9: Long term evolution of the simulated a) bare soil, b) grass and c) tree covers, expressed as the  
750 percentage (%) of Global, NH or SH continental areas, and d) GPP ( $\text{PgC y}^{-1}$ ) over the same regions. Annual mean  
751 values are smoothed by a 100 year running mean.

752

753 Figure 10: Vegetation map comparing a), d), g) the Mid Holocene (first 50 years) and the pre-industrial (50 year  
754 around 1850 CE (last 150 to 100 years) periods of the transient simulation , b), d), h) the differences between  
755 the historical period (last 50 years) and the pre-industrial period of the transient simulation and c), f), i) the  
756 difference between pre-industrial climate for the transient simulation and the PI-Vnone simulations. For  
757 simplicity we only consider bare soil (top), grass (middle) and tree (bottom).

758

759 Figure 11: Long term evolution of Bare soil, Grass and Tree, expressed as the % of land cover North of  $60^\circ \text{N}$ ,  
760 over Eurasia and over West Africa. The different values are plotted as differences with the first 100 year  
761 averages. A 100 years running mean is applied to the curves before plotting.

762

763 Figure 12. Evolution of a) the location of the West African monsoon annual mean (black) and maximum (red)  
764 rain belt in degrees of latitude and b) annual mean (black), minimum (green) and maximum (red) monthly  
765 precipitation ( $\text{mm.d}^{-1}$ ) averages over the Sahel region. The first 100 years have been removed and a 100 years  
766 running mean applied before plotting.

767

768 Figure 13: Evolution of the different tree PFTs in Eurasia, expressed as the percentage change compared to  
769 their 6000 years BP initial state. Each color line stands for a different PFT. Values have been smoothed by a 100  
770 years running mean.

771

772 Figure 14: a) Simulated mega-biome distribution by MH-Vnone, converted from the modelled PFT properties  
773 using the default algorithm described in Figure A1. b) and c) Reconstructions in BIOME 6000 DB version 1 for  
774 the MH and PI periods (Harrison, 2017). d) Number of pixels where reconstruction is available and the model  
775 matches (or does not match) the data. Note that multiple reconstruction sites may be located in the same  
776 model grid cell, in which case we did not group them so that each site was counted once. Numbers in  
777 parenthesis on the x axis in d) represent the number of sites for each biome type. Same as in c) but for the  
778 number of matches between e) the BIOME6000 MH (6k) and PI (0k) reconstructions at pollen sites and f) the  
779 simulated mega-biomes for MH and PI at each model grid cell.

780

781 Figure 15: Impact of the dynamical vegetation and initialization of vegetation on the simulated climate.  
782 Differences for annual mean a) c) e) precipitation ( $\text{mm d}^{-1}$ ) and b) d) f) 2m air temperature ( $^\circ\text{C}$ ) between a) and  
783 b) the MH in the TRHOLV simulation and the MH simulation without dynamical vegetation (MH FPMIP4), c)  
784 and d) the mid Holocene and the pre-industrial simulations in the TRHOLV simulation, and e) and f) the two  
785 pre-industrial simulations initialized from bare soil (PI-Vnone) or a vegetation map for vegetation (PI-Vmap).  
786 See table 2 and text for details on the simulations.

787

788

789 Figure 16: Difference between Vegetation maps obtained with the two different initial states for a) c) e) mid  
790 Holocene simulations, b) d) f) pre-industrial simulations. Vmap stands for MH and PI simulations where the  
791 mid-Holocene vegetation has been initialized from a vegetation map and Vnone for MH and PI simulations  
792 where the mid-Holocene has been initialized from bare soil. For simplicity we only consider fractions of a) b)  
793 bare soil, c) d) grass and e) f) trees.

794

795

796 Figure A1: Parrallel coordinate representation of metrics highlighting model mean bias (left column) and spatial  
797 root mean square differences (right column) against observations for the four climatological seasons  
798 (Decembre to February, djf; Mars to May, mam; June to August, jja ; September to November, son) for surface  
799 air temperature ( $t_{\text{as}}$ ,  $^\circ\text{C}$ ) and precipitation,  $\text{mm d}^{-1}$ ) and Northern Hemisphere extra tropics (NH<sub>EX</sub>,  $20^\circ \text{N}$ - $90^\circ$   
800  $\text{N}$ ), Tropics ( $20^\circ \text{S}$ - $20^\circ \text{N}$ ), and Southern Hemisphere extra tropics (SH<sub>EX</sub>  $90^\circ \text{S}$ - $20^\circ \text{S}$ ). Each color line stands for a  
801 simulations discussed in this manuscript. The results of the different CMIP5 simulations (grey lines) are  
802 included for comparison.

803  
804  
805  
806  
807  
808  
809  
810  
811  
812  
813  
814  
815  
816  
817

Figure A2: (a) Algorithm to convert the modelled PFT properties into the eight megabiomes provided by BIOME 6000 DB version 1. The default thresholds (in black) are the same as Zhu et al. (2018), while different values (in red) are tested:  $GDD_5$  (annual growing degree days above 5 °C) of 500 K days (Joos et al., 2004), FPC (foliage projective cover) of 0.3 and 0.6 (Prentice et al., 2011) Height (average height of all existing tree PFTs) of 10 m (Prentice et al., 2011). (b) Simulated megabiome distribution by MH\_Vnone and MH\_Vmap, using different conversion methods in (a). (c) and (d) The number of pixels where modelled megabiome matches data for each biome type, divided by the total number of available sites for that biome type, for mid-Holocene compared with BIOME 6000 6ka (c) and for pre-industrial compared with BIOME 6000 0ka (d).

- 819  
820 Abis, B. and Brovkin, V.: Environmental conditions for alternative tree-cover states in high latitudes,  
821 *Biogeosciences*, 14, 511-527, 2017.
- 822 Albani, S., Mahowald, N. M., Winckler, G., Anderson, R. F., Bradtmiller, L. I., Delmonte, B., François,  
823 R., Goman, M., Heavens, N. G., Hesse, P. P., Hovan, S. A., Kang, S. G., Kohfeld, K. E., Lu, H., Maggi, V.,  
824 Mason, J. A., Mayewski, P. A., McGee, D., Miao, X., Otto-Bliesner, B. L., Perry, A. T., Pourmand, A.,  
825 Roberts, H. M., Rosenbloom, N., Stevens, T., and Sun, J.: Twelve thousand years of dust: the  
826 Holocene global dust cycle constrained by natural archives, *Clim. Past*, 11, 869-903, 2015.
- 827 Alexandrov, D. V., Bashkirtseva, I. A., and Ryashko, L. B.: Noise-induced transitions and shifts in a  
828 climate–vegetation feedback model, *Royal Society Open Science*, 5, 2018.
- 829 Aumont, O. and Bopp, L.: Globalizing results from ocean in situ iron fertilization studies, *Global*  
830 *Biogeochemical Cycles*, 20, -, 2006.
- 831 Bartlein, P. J., Harrison, S. P., Brewer, S., Connor, S., Davis, B. A. S., Gajewski, K., Guiot, J., Harrison-  
832 Prentice, T. I., Henderson, A., Peyron, O., Prentice, I. C., Scholze, M., Seppa, H., Shuman, B., Sugita,  
833 S., Thompson, R. S., Viau, A. E., Williams, J., and Wu, H.: Pollen-based continental climate  
834 reconstructions at 6 and 21 ka: a global synthesis, *Climate Dynamics*, 37, 775-802, 2011.
- 835 Bathiany, S., Claussen, M., and Fraedrich, K.: Implications of climate variability for the detection of  
836 multiple equilibria and for rapid transitions in the atmosphere-vegetation system, *Climate*  
837 *Dynamics*, 38, 1775-1790, 2012.
- 838 Berger, A.: Long-term variations of caloric solar radiation resulting from the Earth's orbital elements,  
839 *Quaternary Research*, 9, 139-167, 1978.
- 840 Bigelow, N. H., Brubaker, L. B., Edwards, M. E., Harrison, S. P., Prentice, I. C., Anderson, P. M.,  
841 Andreev, A. A., Bartlein, P. J., Christensen, T. R., Cramer, W., Kaplan, J. O., Lozhkin, A. V.,  
842 Matveyeva, N. V., Murray, D. F., McGuire, A. D., Razzhivin, V. Y., Ritchie, J. C., Smith, B., Walker, D.  
843 A., Gajewski, K., Wolf, V., Holmqvist, B. H., Igarashi, Y., Kremenetskii, K., Paus, A., Pisaric, M. F. J.,  
844 and Volkova, V. S.: Climate change and Arctic ecosystems: 1. Vegetation changes north of 55  
845 degrees N between the last glacial maximum, mid-Holocene, and present, *Journal of Geophysical*  
846 *Research-Atmospheres*, 108, 2003.
- 847 Boisier, J., Noblet - Ducoudré, N. d., Pitman, A., Cruz, F., Delire, C., den Hurk, B., Molen, M., Müller,  
848 C., and Voltaire, A.: Attributing the impacts of land - cover changes in temperate regions on  
849 surface temperature and heat fluxes to specific causes: Results from the first LUCID set of  
850 simulations, *Journal of Geophysical Research: Atmospheres*, 117, 2012.
- 851 Bonfils, C., de Noblet-Ducoure, N., Braconnot, P., and Joussaume, S.: Hot desert albedo and climate  
852 change: Mid-Holocene monsoon in North Africa, *Journal of Climate*, 14, 3724-3737, 2001.
- 853 Braconnot, P., Harrison, S. P., Kageyama, M., Bartlein, P. J., Masson-Delmotte, V., Abe-Ouchi, A.,  
854 Otto-Bliesner, B., and Zhao, Y.: Evaluation of climate models using palaeoclimatic data, *Nature*  
855 *Climate Change*, 2, 417-424, 2012.
- 856 Braconnot, P., Joussaume, S., Marti, O., and de Noblet, N.: Synergistic feedbacks from ocean and  
857 vegetation on the African monsoon response to mid-Holocene insolation, *Geophys .Res. Lett.*, 26,  
858 2481-2484, 1999.
- 859 Braconnot, P. and Kageyama, M.: Shortwave forcing and feedbacks in Last Glacial Maximum and Mid-  
860 Holocene PMIP3 simulations, *Phil. Trans. R. Soc. A*, 373, 20140424, 2015.
- 861 Braconnot, P., Marti, O., and Joussaume, S.: Adjustment and feedbacks in a global coupled ocean-  
862 atmosphere model, *Climate Dynamics*, 13, 507-519, 1997.
- 863 Braconnot, P., Otto-Bliesner, B., Harrison, S., Joussaume, S., Peterchmitt, J. Y., Abe-Ouchi, A., Crucifix,  
864 M., Driesschaert, E., Fichet, T., Hewitt, C. D., Kageyama, M., Kitoh, A., Laine, A., Loutre, M. F.,  
865 Marti, O., Merkel, U., Ramstein, G., Valdes, P., Weber, S. L., Yu, Y., and Zhao, Y.: Results of PMIP2  
866 coupled simulations of the Mid-Holocene and Last Glacial Maximum - Part 1: experiments and  
867 large-scale features, *Climate of the Past*, 3, 261-277, 2007a.

868 Braconnot, P., Otto-Bliesner, B., Harrison, S., Joussaume, S., Peterchmitt, J. Y., Abe-Ouchi, A., Crucifix,  
869 M., Driesschaert, E., Fichefet, T., Hewitt, C. D., Kageyama, M., Kitoh, A., Loutre, M. F., Marti, O.,  
870 Merkel, U., Ramstein, G., Valdes, P., Weber, L., Yu, Y., and Zhao, Y.: Results of PMIP2 coupled  
871 simulations of the Mid-Holocene and Last Glacial Maximum - Part 2: feedbacks with emphasis on  
872 the location of the ITCZ and mid- and high latitudes heat budget, *Climate of the Past*, 3, 279-296,  
873 2007b.

874 Brovkin, V., Bendtsen, J., Claussen, M., Ganopolski, A., Kubatzki, C., Petoukhov, V., and Andreev, A.:  
875 Carbon cycle, vegetation, and climate dynamics in the Holocene: Experiments with the CLIMBER-2  
876 model, *Global Biogeochemical Cycles*, 16, 2002.

877 Campbell, J. E., Berry, J. A., Seibt, U., Smith, S. J., Montzka, S. A., Launois, T., Belviso, S., Bopp, L., and  
878 Laine, M.: Large historical growth in global terrestrial gross primary production, *Nature*, 544, 84,  
879 2017.

880 Claussen, M.: Late Quaternary vegetation-climate feedbacks, *Climate of the Past*, 5, 203-216, 2009.

881 Claussen, M. and Gayler, V.: The greening of the Sahara during the mid-Holocene: results of an  
882 interactive atmosphere-biome model, *Global Ecology and Biogeography Letters*, 6, 369-377, 1997.

883 COHMAP-Members: Climatic changes of the last 18,000 years: observations and model simulations,  
884 *Science*, 241, 1043-1052, 1988.

885 Crucifix, M., Loutre, M. F., Tulkens, P., Fichefet, T., and Berger, A.: Climate evolution during the  
886 Holocene: a study with an Earth system model of intermediate complexity, *Climate Dynamics*, 19,  
887 43-60, 2002.

888 d'Orgeval, T., Polcher, J., and de Rosnay, P.: Sensitivity of the West African hydrological cycle in  
889 ORCHIDEE to infiltration processes, *Hydrol. Earth Syst. Sci.*, 12, 1387-1401, 2008.

890 Dallmeyer, A., Claussen, M., and Brovkin, V.: Harmonising plant functional type distributions for  
891 evaluating Earth system models, *Clim. Past*, 15, 335-366, 2019.

892 Dallmeyer, A., Claussen, M., and Otto, J.: Contribution of oceanic and vegetation feedbacks to  
893 Holocene climate change in monsoonal Asia, *Clim. Past*, 6, 195-218, 2010.

894 Davis, B. A. S., Brewer, S., Stevenson, A. C., and Guiot, J.: The temperature of Europe during the  
895 Holocene reconstructed from pollen data, *Quaternary Science Reviews*, 22, 1701-1716, 2003.

896 de Noblet-Ducoudre, N., Claussen, R., and Prentice, C.: Mid-Holocene greening of the Sahara: first  
897 results of the GAIM 6000 year BP Experiment with two asynchronously coupled atmosphere/biome  
898 models, *Climate Dynamics*, 16, 643-659, 2000.

899 de Noblet, N., Prentice, I. C., Joussaume, S., Texier, D., Botta, A., and Haxeltine, A.: Possible role of  
900 atmosphere-biosphere interactions in triggering the last glaciation, *Geophys. Res. Letters*, 23, 3191-  
901 3194, 1996.

902 de Rosnay, P., Polcher, J., Bruen, M., and Laval, K.: Impact of a physically based soil water flow and  
903 soil-plant interaction representation for modeling large-scale land surface processes, *Journal of*  
904 *Geophysical Research-Atmospheres*, 107, 2002.

905 deMenocal, P., Ortiz, J., Guilderson, T., Adkins, J., Sarnthein, M., Baker, L., and Yarusinsky, M.: Abrupt  
906 onset and termination of the African Humid Period: rapid climate responses to gradual insolation  
907 forcing, *Quaternary Science Reviews*, 19, 347-361, 2000.

908 Ducoudré, N., Laval, K., and Perrier, A.: SECHIBA, a new set of parameterizations of the hydrologic  
909 exchanges at the land/atmosphere interface within the LMD atmospheric general circulation  
910 model, *Journal of Climate*, 6, 1993.

911 Dufresne, J. L., Foujols, M. A., Denvil, S., Caubel, A., Marti, O., Aumont, O., Balkanski, Y., Bekki, S.,  
912 Bellenger, H., Benschila, R., Bony, S., Bopp, L., Braconnot, P., Brockmann, P., Cadule, P., Cheruy, F.,  
913 Codron, F., Cozic, A., Cugnet, D., de Noblet, N., Duvel, J. P., Ethe, C., Fairhead, L., Fichefet, T.,  
914 Flavoni, S., Friedlingstein, P., Grandpeix, J. Y., Guez, L., Guilyardi, E., Hauglustaine, D., Hourdin, F.,  
915 Idelkadi, A., Ghattas, J., Joussaume, S., Kageyama, M., Krinner, G., Labetoulle, S., Lahellec, A.,  
916 Lefebvre, M. P., Lefevre, F., Levy, C., Li, Z. X., Lloyd, J., Lott, F., Madec, G., Mancip, M., Marchand,  
917 M., Masson, S., Meurdesoif, Y., Mignot, J., Musat, I., Parouty, S., Polcher, J., Rio, C., Schulz, M.,  
918 Swingedouw, D., Szopa, S., Talandier, C., Terray, P., Viovy, N., and Vuichard, N.: Climate change

919 projections using the IPSL-CM5 Earth System Model: from CMIP3 to CMIP5, *Climate Dynamics*, 40,  
920 2123-2165, 2013.

921 Egerer, S., Claussen, M., Reick, C., and Stanelle, T.: Could gradual changes in Holocene Saharan  
922 landscape have caused the observed abrupt shift in North Atlantic dust deposition?, *Earth and*  
923 *Planetary Science Letters*, 473, 104-112, 2017.

924 Fichefet, T. and Maqueda, M. A. M.: Modelling the influence of snow accumulation and snow-ice  
925 formation on the seasonal cycle of the Antarctic sea-ice cover, *Climate Dynamics*, 15, 251-268,  
926 1999.

927 Gleckler, P., Doutriaux, C., Durack, P., Taylor, K., Zhang, Y., Williams, D., Mason, E., and Servonnat, J.:  
928 A More Powerful Reality Test for Climate Models, *EOS, Transactions of the American Geophysical*  
929 *Union*, 97, 2016.

930 Guimberteau, M., Zhu, D., Maignan, F., Huang, Y., Yue, C., Dantec-Nédélec, S., Ottlé, C., Jornet-Puig,  
931 A., Bastos, A., Laurent, P., Goll, D., Bowring, S., Chang, J., Guenet, B., Tifafi, M., Peng, S., Krinner, G.,  
932 Ducharne, A., Wang, F., Wang, T., Wang, X., Wang, Y., Yin, Z., Lauerwald, R., Joetzjer, E., Qiu, C.,  
933 Kim, H., and Ciais, P.: ORCHIDEE-MICT (v8.4.1), a land surface model for the high latitudes: model  
934 description and validation, *Geosci. Model Dev.*, 11, 121-163, 2018.

935 Harrison, S.: BIOME 6000 DB classified plotfile version 1, University of Reading. Dataset. , doi:  
936 <http://dx.doi.org/10.17864/1947.99>, 2017. 2017.

937 Harrison, S. P., Bartlein, P. J., Brewer, S., Prentice, I. C., Boyd, M., Hessler, I., Holmgren, K., Izumi, K.,  
938 and Willis, K.: Climate model benchmarking with glacial and mid-Holocene climates, *Climate*  
939 *Dynamics*, 43, 671-688, 2014.

940 Harrison, S. P., Jolly, D., Laarif, F., Abe-Ouchi, A., Dong, B., Herterich, K., Hewitt, C., Joussaume, S.,  
941 Kutzbach, J. E., Mitchell, J., de Noblet, N., and Valdes, P.: Intercomparison of Simulated Global  
942 Vegetation Distributions in Response to 6 kyr BP Orbital Forcing, *Journal of Climate*, 11, 2721-2742,  
943 1998.

944 Held, I. M. and Soden, B. J.: Robust Responses of the Hydrological Cycle to Global Warming, *Journal*  
945 *of Climate*, 19, 5686-5699, 2006.

946 Hély, C. and Lézine, A.-M.: Holocene changes in African vegetation: tradeoff between climate and  
947 water availability, *Climate of the Past*, 10, 681-686, 2014.

948 Hopcroft, P. O., Valdes, P. J., Harper, A. B., and Beerling, D. J.: Multi vegetation model evaluation of  
949 the Green Sahara climate regime, *Geophysical Research Letters*, 44, 6804-6813, 2017.

950 Hourdin, F., Foujols, M. A., Codron, F., Guemas, V., Dufresne, J. L., Bony, S., Denvil, S., Guez, L., Lott,  
951 F., Ghattas, J., Braconnot, P., Marti, O., Meurdesoif, Y., and Bopp, L.: Impact of the LMDZ  
952 atmospheric grid configuration on the climate and sensitivity of the IPSL-CM5A coupled model,  
953 *Climate Dynamics*, 40, 2167-2192, 2013.

954 Jansen, E., Overpeck, J., Briffa, K. R., Duplessy, J. C., Joos, F., Masson-Delmotte, V., Olago, D., Otto-  
955 Bliesner, B., Peltier, W. R., Rahmstorf, S., Ramesh, R., Raynaud, D., Rind, D., Solomina, O., Villalba,  
956 R., and Zhang, D.: Paleoclimate. In: *Climate Change 2007: The Physical Science Basis. Contribution of*  
957 *Working Group I to the Fourth Assessment Report of the Intergovernmental Panel on Climate*  
958 *Change*, Solomon, S., Qin, D. H., Manning, M., Chen, Z., Marsuis, M., Averyt, K. B., Tignor, M., and  
959 Miller, H. L. (Eds.), Cambridge University Press, Cambridge, United Kingdom and New York, NY, USA,  
960 2007.

961 Jolly, D., Prentice, I. C., Bonnefille, R., Ballouche, A., Bengo, M., Brenac, P., Buchet, G., Burney, D.,  
962 Cazet, J.-P., Cheddadi, R., Edohr, T., Elenga, H., Elmoutaki, S., Guiot, J., Laarif, F., Lamb, H., Lézine,  
963 A.-M., Maley, J., Mbenza, M., Peyron, O., Reille, M., Reynaud-Ferrera, I., Riollet, G., Ritchie, J. C.,  
964 Roche, E., Scott, L., Ssemmanda, I., Straka, H., Umer, M., Van Campo, E., Vilimumbala, S., Vincens,  
965 A., and Waller, M.: Biome reconstruction from pollen and plant macrofossil data for Africa and the  
966 Arabian peninsula at 0 and 6 ka., *Journal of Biogeography*, 25, 1007-1028, 1998.

967 Jomelli, V., Khodri, M., Favier, V., Brunstein, D., Ledru, M. P., Wagnon, P., Blard, P. H., Sicart, J. E.,  
968 Braucher, R., Grancher, D., Bourles, D. L., Braconnot, P., and Vuille, M.: Irregular tropical glacier  
969 retreat over the Holocene epoch driven by progressive warming, *Nature*, 474, 196-199, 2011.

970 Joos, F., Gerber, S., Prentice, I., Otto-Bliesner, B., and Valdes, P.: Transient simulations of Holocene  
971 atmospheric carbon dioxide and terrestrial carbon since the Last Glacial Maximum, *GLOBAL*  
972 *BIOGEOCHEMICAL CYCLES*, 18, -, 2004.

973 Joos, F. and Spahni, R.: Rates of change in natural and anthropogenic radiative forcing over the past  
974 20,000 years, *Proceedings of the National Academy of Sciences*, 105, 1425-1430, 2008.

975 Joussaume, S. and Braconnot, P.: Sensitivity of paleoclimate simulation results to season definitions,  
976 *J. Geophys. Res.*, 102, 1943-1956, 1997.

977 Joussaume, S., Taylor, K. E., Braconnot, P., Mitchell, J. F. B., Kutzbach, J. E., Harrison, S. P., Prentice, I.  
978 C., Broccoli, A. J., Abe-Ouchi, A., Bartlein, P. J., Bonfils, C., Dong, B., Guiot, J., Herterich, K., Hewitt, C.  
979 D., Jolly, D., Kim, J. W., Kislov, A., Kitoh, A., Loutre, M. F., Masson, V., McAvaney, B., McFarlane, N.,  
980 de Noblet, N., Peltier, W. R., Peterschmitt, J. Y., Pollard, D., Rind, D., Royer, J. F., Schlesinger, M. E.,  
981 Syktus, J., Thompson, S., Valdes, P., Vettoretti, G., Webb, R. S., and Wypytta, U.: Monsoon changes  
982 for 6000 years ago: Results of 18 simulations from the Paleoclimate Modeling Intercomparison  
983 Project (PMIP), *Geophysical Research Letters*, 26, 859-862, 1999.

984 Kageyama, M., Braconnot, P., Bopp, L., Caubel, A., Foujols, M. A., Guilyardi, E., Khodri, M., Lloyd, J.,  
985 Lombard, F., Mariotti, V., Marti, O., Roy, T., and Woillez, M. N.: Mid-Holocene and Last Glacial  
986 Maximum climate simulations with the IPSL model-part I: comparing IPSL\_CM5A to IPSL\_CM4,  
987 *Climate Dynamics*, 40, 2447-2468, 2013a.

988 Kageyama, M., Braconnot, P., Bopp, L., Mariotti, V., Roy, T., Woillez, M. N., Caubel, A., Foujols, M. A.,  
989 Guilyardi, E., Khodri, M., Lloyd, J., Lombard, F., and Marti, O.: Mid-Holocene and last glacial  
990 maximum climate simulations with the IPSL model: part II: model-data comparisons, *Climate*  
991 *Dynamics*, 40, 2469-2495, 2013b.

992 Kageyama, M., Braconnot, P., Harrison, S. P., Haywood, A. M., Jungclaus, J. H., Otto-Bliesner, B. L.,  
993 Peterschmitt, J. Y., Abe-Ouchi, A., Albani, S., Bartlein, P. J., Brierley, C., Crucifix, M., Dolan, A.,  
994 Fernandez-Donado, L., Fischer, H., Hopcroft, P. O., Ivanovic, R. F., Lambert, F., Lunt, D. J.,  
995 Mahowald, N. M., Peltier, W. R., Phipps, S. J., Roche, D. M., Schmidt, G. A., Tarasov, L., Valdes, P. J.,  
996 Zhang, Q., and Zhou, T.: The PMIP4 contribution to CMIP6 – Part 1: Overview and over-arching  
997 analysis plan, *Geosci. Model Dev.*, 11, 1033-1057, 2018.

998 Krinner, G., Viovy, N., de Noblet-Ducoudre, N., Ogee, J., Polcher, J., Friedlingstein, P., Ciais, P., Sitch,  
999 S., and Prentice, I. C.: A dynamic global vegetation model for studies of the coupled atmosphere-  
1000 biosphere system, *Global Biogeochemical Cycles*, 19, -, 2005.

1001 Kutzbach, J. E., Bartlein, P. J., Foley, J. A., Harrison, S. P., Hostetler, S. W., Liu, Z., Prentice, I. C., and  
1002 Webb, T.: Potential role of vegetation feedback in the climate sensitivity of high-latitude regions: A  
1003 case study at 6000 years BP, *Global Biogeochemical Cycles*, 10, 727-736, 1996.

1004 Lenton, T. M., Held, H., Kriegler, E., Hall, J. W., Lucht, W., Rahmstorf, S., and Schellnhuber, H. J.:  
1005 Tipping elements in the Earth's climate system, *Proceedings of the National Academy of Sciences*,  
1006 105, 1786-1793, 2008.

1007 Levis, S., Bonan, G. B., and Bonfils, C.: Soil feedback drives the mid-Holocene North African monsoon  
1008 northward in fully coupled CCSM2 simulations with a dynamic vegetation model, *Climate Dynamics*,  
1009 23, 791-802, 2004.

1010 Lezine, A. M., Hely, C., Grenier, C., Braconnot, P., and Krinner, G.: Sahara and Sahel vulnerability to  
1011 climate changes, lessons from Holocene hydrological data, *Quaternary Science Reviews*, 30, 3001-  
1012 3012, 2011.

1013 Lezine, A. M., Ivory, S. J., Braconnot, P., and Marti, O.: Timing of the southward retreat of the ITCZ at  
1014 the end of the Holocene Humid Period in Southern Arabia: Data-model comparison, *Quaternary*  
1015 *Science Reviews*, 164, 68-76, 2017.

1016 Liu, Z., Wang, Y., Gallimore, R., Gasse, F., Johnson, T., deMenocal, P., Adkins, J., Notaro, M., Prentice,  
1017 I. C., Kutzbach, J., Jacob, R., Behling, P., Wang, L., and Ong, E.: Simulating the transient evolution  
1018 and abrupt change of Northern Africa atmosphere-ocean-terrestrial ecosystem in the Holocene,  
1019 *Quaternary Science Reviews*, 26, 1818-1837, 2007.

1020 Liu, Z. Y., Zhu, J., Rosenthal, Y., Zhang, X., Otto-Bliesner, B. L., Timmermann, A., Smith, R. S., Lohmann,  
1021 G., Zheng, W. P., and Timm, O. E.: The Holocene temperature conundrum, *Proceedings of the*  
1022 *National Academy of Sciences of the United States of America*, 111, E3501-E3505, 2014.

1023 Madec, G.: NEMO ocean engine, 2008.

1024 Marsicek, J., Shuman, B. N., Bartlein, P. J., Shafer, S. L., and Brewer, S.: Reconciling divergent trends  
1025 and millennial variations in Holocene temperatures, *Nature*, 554, 92, 2018.

1026 Marti, O., Braconnot, P., Dufresne, J. L., Bellier, J., Benschila, R., Bony, S., Brockmann, P., Cadule, P.,  
1027 Caubel, A., Codron, F., de Noblet, N., Denvil, S., Fairhead, L., Fichet, T., Foujols, M. A.,  
1028 Friedlingstein, P., Goosse, H., Grandpeix, J. Y., Guilyardi, E., Hourdin, F., Idelkadi, A., Kageyama, M.,  
1029 Krinner, G., Levy, C., Madec, G., Mignot, J., Musat, I., Swingedouw, D., and Talandier, C.: Key  
1030 features of the IPSL ocean atmosphere model and its sensitivity to atmospheric resolution, *Climate*  
1031 *Dynamics*, 34, 1-26, 2010.

1032 Mauri, A., Davis, B., Collins, P., and Kaplan, J.: The climate of Europe during the Holocene: a gridded  
1033 pollen-based reconstruction and its multi-proxy evaluation, *Quaternary Science Reviews*, 112, 109-  
1034 127, 2015.

1035 Otto-Bliesner, B., Braconnot, P., Harrison, S., Lunt, D., Abe-Ouchi, A., Albani, S., Bartlein, P., Capron,  
1036 E., Carlson, A., Dutton, A., Fischer, H., Goelzer, H., Govin, A., Haywood, A., Joos, F., LeGrande, A.,  
1037 Lipscomb, W., Lohmann, G., Mahowald, N., Nehrbass-Ahles, C., Pausata, F., Peterschmitt, J.-Y.,  
1038 Phipps, S., Renssen, H., and Zhang, Q.: The PMIP4 contribution to CMIP6 – Part 2: Two interglacials,  
1039 scientific objective and experimental design for Holocene and Last Interglacial simulations,  
1040 *Geoscientific Model Development*, 10, 3979-4003, 2017.

1041 Otto, J., Raddatz, T., and Claussen, M.: Strength of forest-albedo feedback in mid-Holocene climate  
1042 simulations, *Clim. Past*, 7, 1027-1039, 2011.

1043 Otto, J., Raddatz, T., Claussen, M., Brovkin, V., and Gayler, V.: Separation of atmosphere-ocean-  
1044 vegetation feedbacks and synergies for mid-Holocene climate, *Geophysical Research Letters*, 36,  
1045 2009.

1046 Pausata, F. S., Messori, G., and Zhang, Q.: Impacts of dust reduction on the northward expansion of  
1047 the African monsoon during the Green Sahara period, *Earth and Planetary Science Letters*, 434,  
1048 298-307, 2016.

1049 Prentice, I. C., Harrison, S. P., and Bartlein, P. J.: Global vegetation and terrestrial carbon cycle  
1050 changes after the last ice age, *New Phytologist*, 189, 988-998, 2011.

1051 Prentice, I. C. and Webb, T.: BIOME 6000: reconstructing global mid-Holocene vegetation patterns  
1052 from palaeoecological records, *Journal of Biogeography*, 25, 997-1005, 1998.

1053 Renssen, H., Seppä, H., Crosta, X., Goosse, H., and Roche, D. M.: Global characterization of the  
1054 Holocene Thermal Maximum, *Quaternary Science Reviews*, 48, 7-19, 2012.

1055 Saint-Lu, M., Braconnot, P., Leloup, J., and Marti, O.: The role of El Niño in the global energy  
1056 redistribution: a case study in the mid-Holocene, *Climate Dynamics*, 2016. 1-18, 2016.

1057 Scheffer, M., Hirota, M., Holmgren, M., Van Nes, E. H., and Chapin, F. S.: Thresholds for boreal biome  
1058 transitions, *Proceedings of the National Academy of Sciences*, 109, 21384-21389, 2012.

1059 Singarayer, J. S. and Valdes, P. J.: High-latitude climate sensitivity to ice-sheet forcing over the last  
1060 120 kyr, *Quaternary Science Reviews*, 29, 43-55, 2010.

1061 Texier, D., de Noblet, N., Harrison, S. P., Haxeltine, A., Jolly, D., Joussaume, S., Laarif, F., Prentice, I. C.,  
1062 and Tarasov, P.: Quantifying the role of biosphere-atmosphere feedbacks in climate change:  
1063 coupled model simulations for 6000 years BP and comparison with palaeodata for northern Eurasia  
1064 and northern Africa, *Climate Dynamics*, 13, 865-882, 1997.

1065 Torres, O., Braconnot, P., Marti, O., and Gentil, L.: Impact of air-sea drag coefficient for latent heat  
1066 flux on large scale climate in coupled and atmosphere stand-alone simulations, *Climate Dynamics*,  
1067 2018. 1-20, 2018.

1068 Valcke, S.: OASIS3 user's guide (prism-2-5). CERFACS, Toulouse, France, 2006.

1069 Vial, J., Dufresne, J. L., and Bony, S.: On the interpretation of inter-model spread in CMIP5 climate  
1070 sensitivity estimates, *Climate Dynamics*, 41, 3339-3362, 2013.

1071 Wang, T., Ottlé, C., Boone, A., Ciais, P., Brun, E., Morin, S., Krinner, G., Piao, S., and Peng, S.:  
1072 Evaluation of an improved intermediate complexity snow scheme in the ORCHIDEE land surface  
1073 model, *Journal of Geophysical Research: Atmospheres*, 118, 6064-6079, 2013.

1074 Wanner, H., Beer, J., Buetikofer, J., Crowley, T. J., Cubasch, U., Flueckiger, J., Goosse, H., Grosjean,  
1075 M., Joos, F., Kaplan, J. O., Kuettel, M., Mueller, S. A., Prentice, I. C., Solomina, O., Stocker, T. F.,  
1076 Tarasov, P., Wagner, M., and Widmann, M.: Mid- to Late Holocene climate change: an overview,  
1077 *Quaternary Science Reviews*, 27, 1791-1828, 2008.

1078 Wohlfahrt, J., Harrison, S. P., and Braconnot, P.: Synergistic feedbacks between ocean and vegetation  
1079 on mid- and high-latitude climates during the mid-Holocene, *Climate Dynamics*, 22, 223-238, 2004.

1080 Woillez, M., Kageyama, M., Krinner, G., De Noblet-Ducoudré, N., Viovy, N., and Mancip, M.: Impact of  
1081 CO<sub>2</sub> and climate on the Last Glacial Maximum vegetation: results from the ORCHIDEE/IPSL models,  
1082 *Climate of the Past*, 7, 557-577, 2011.

1083 Zhu, D., Ciais, P., Chang, J., Krinner, G., Peng, S., Viovy, N., Peñuelas, J., and Zimov, S.: The large mean  
1084 body size of mammalian herbivores explains the productivity paradox during the Last Glacial  
1085 Maximum, *Nature Ecology & Evolution*, 2, 640-649, 2018.

1086 Zhu, D., Peng, S. S., Ciais, P., Viovy, N., Druel, A., Kageyama, M., Krinner, G., Peylin, P., Ottlé, C., Piao,  
1087 S. L., Poulter, B., Schepaschenko, D., and Shvidenko, A.: Improving the dynamics of Northern  
1088 Hemisphere high-latitude vegetation in the ORCHIDEE ecosystem model, *Geoscientific Model  
1089 Development*, 8, 2263-2283, 2015.

1090  
1091

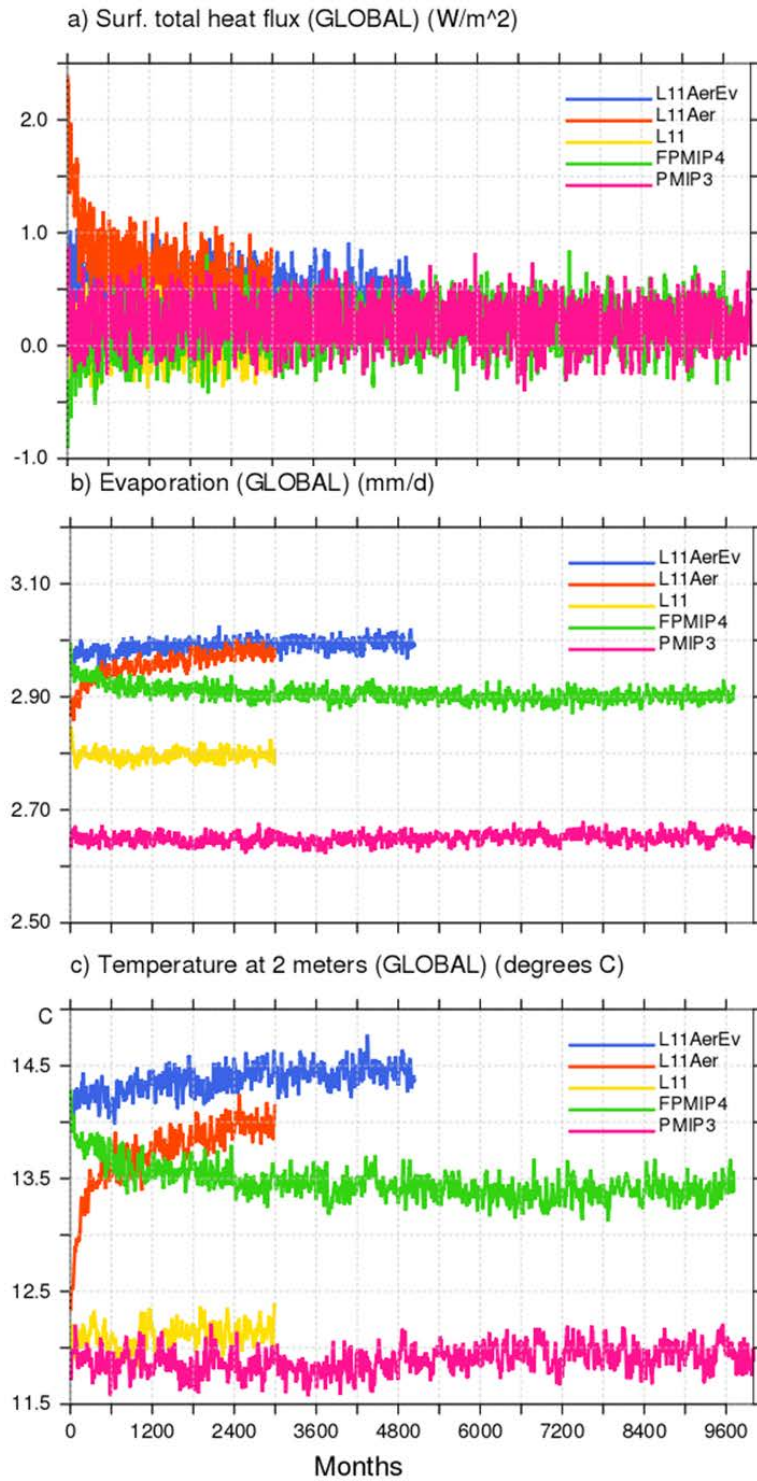


Figure 1:

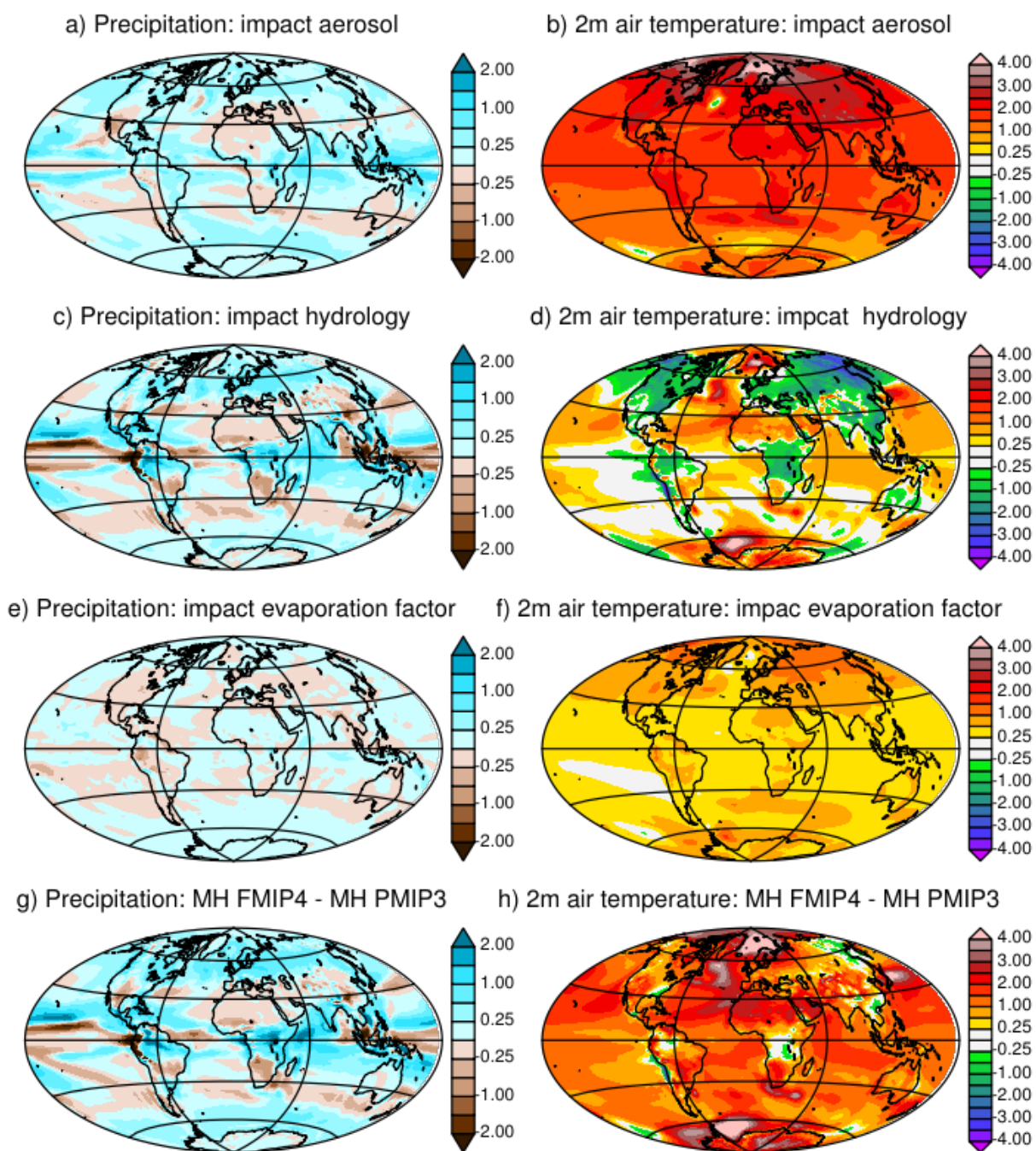
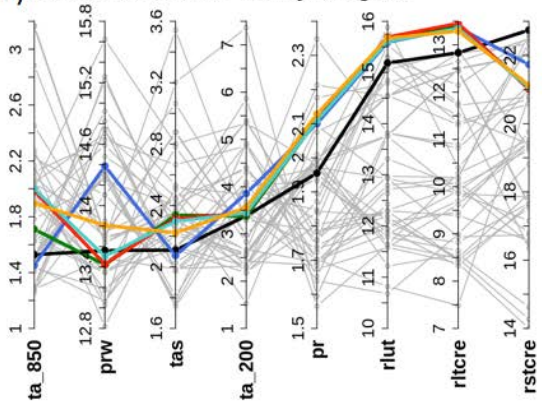
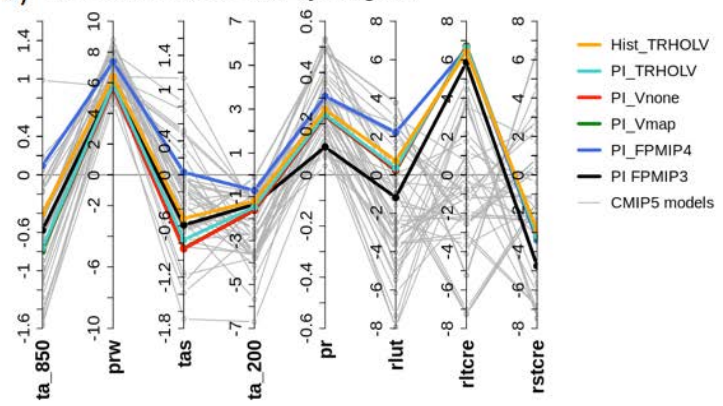


Figure 2:

a) Parallel coordinates - rms\_xy ann global



b) Parallel coordinates - bias\_xy ann global



- Hist\_TRHOLV
- PI\_TRHOLV
- PI\_Vnone
- PI\_Vmap
- PI\_FPMIP4
- PI\_FPMIP3
- CMIP5 models

Figure 3.

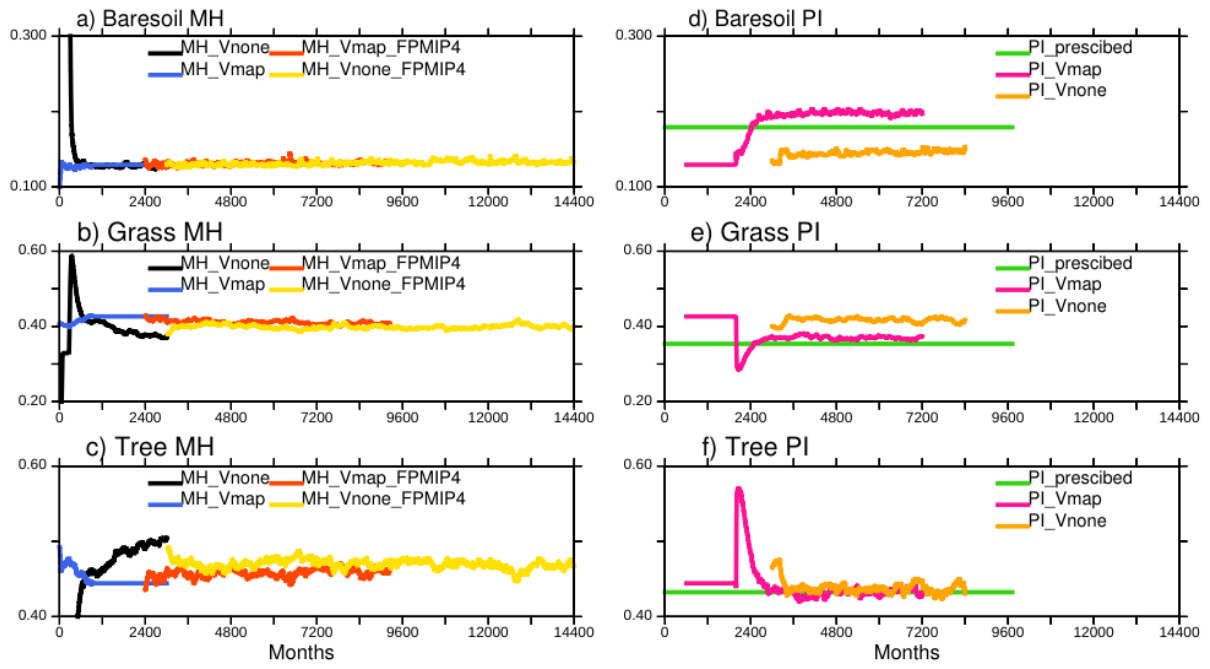


Figure 4.

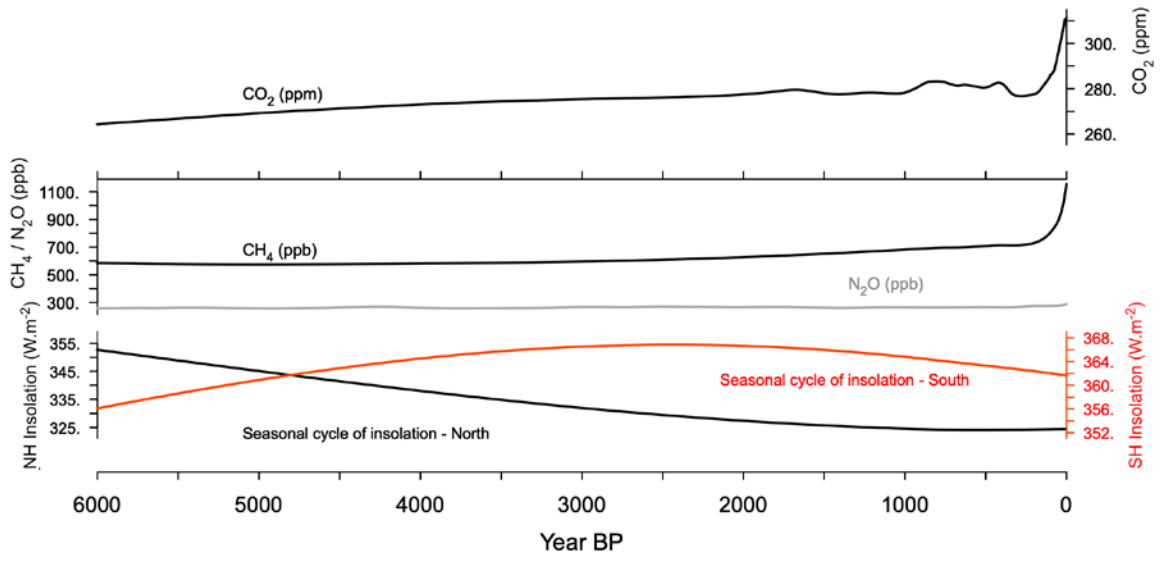


Figure 5:

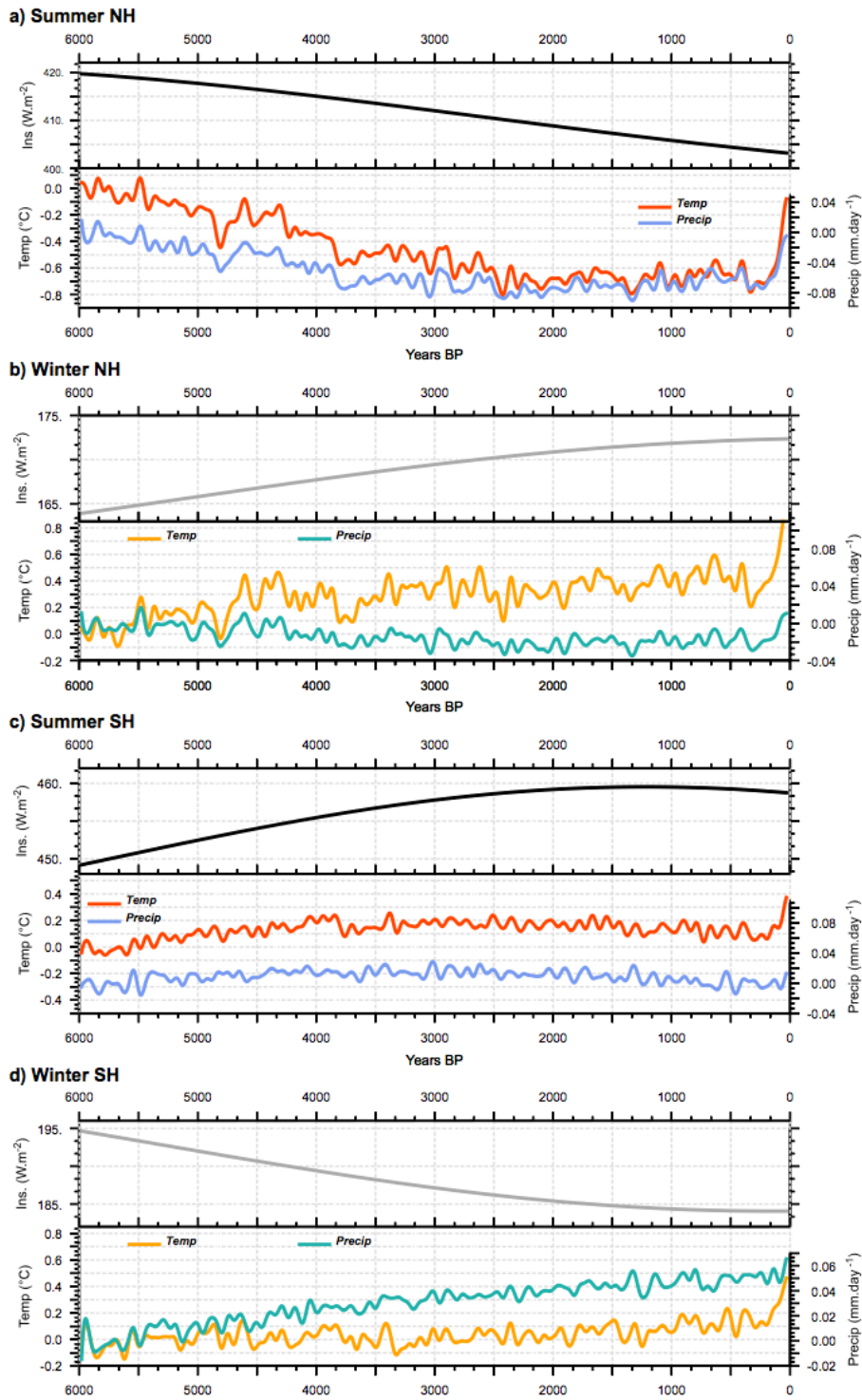


Figure 6

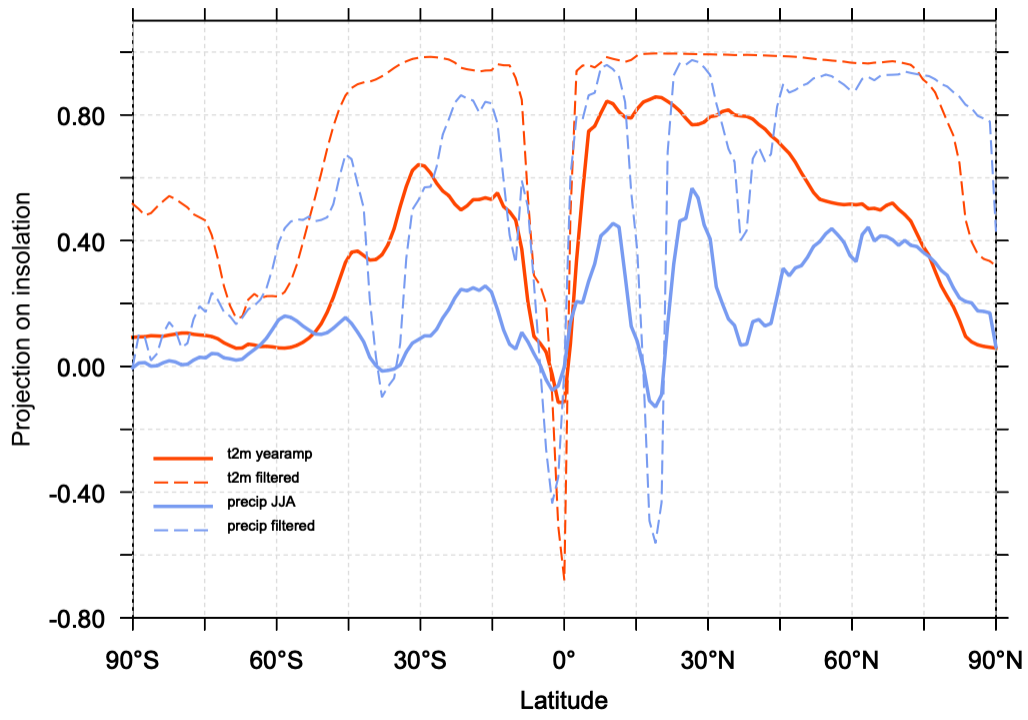


Figure 7:

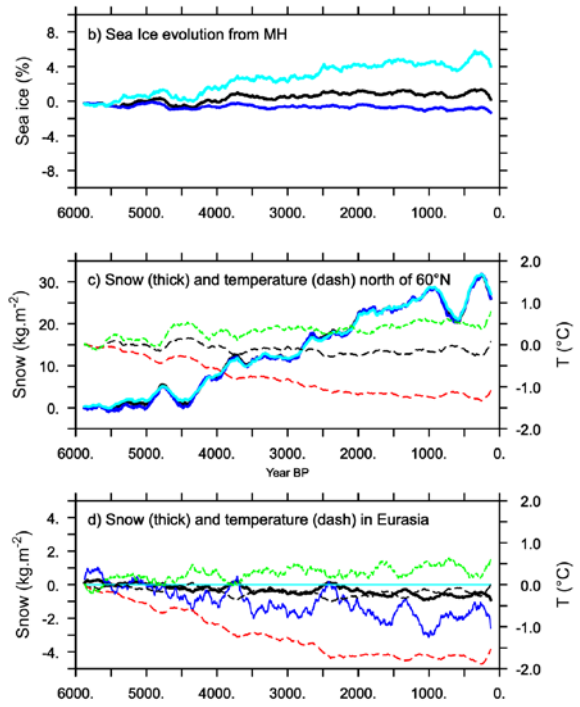
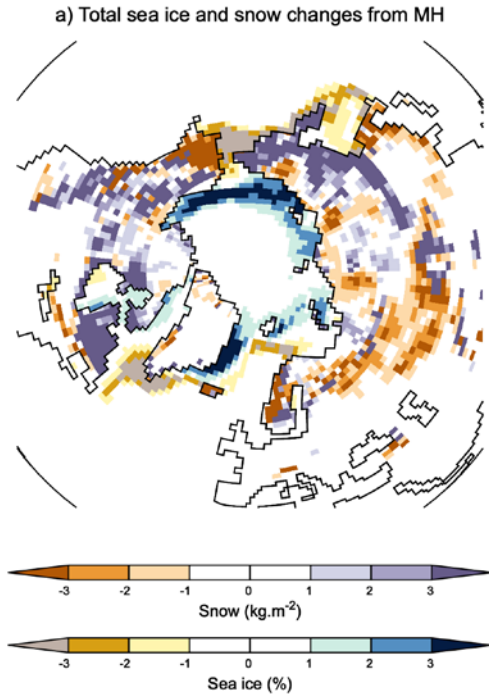


Figure 8:

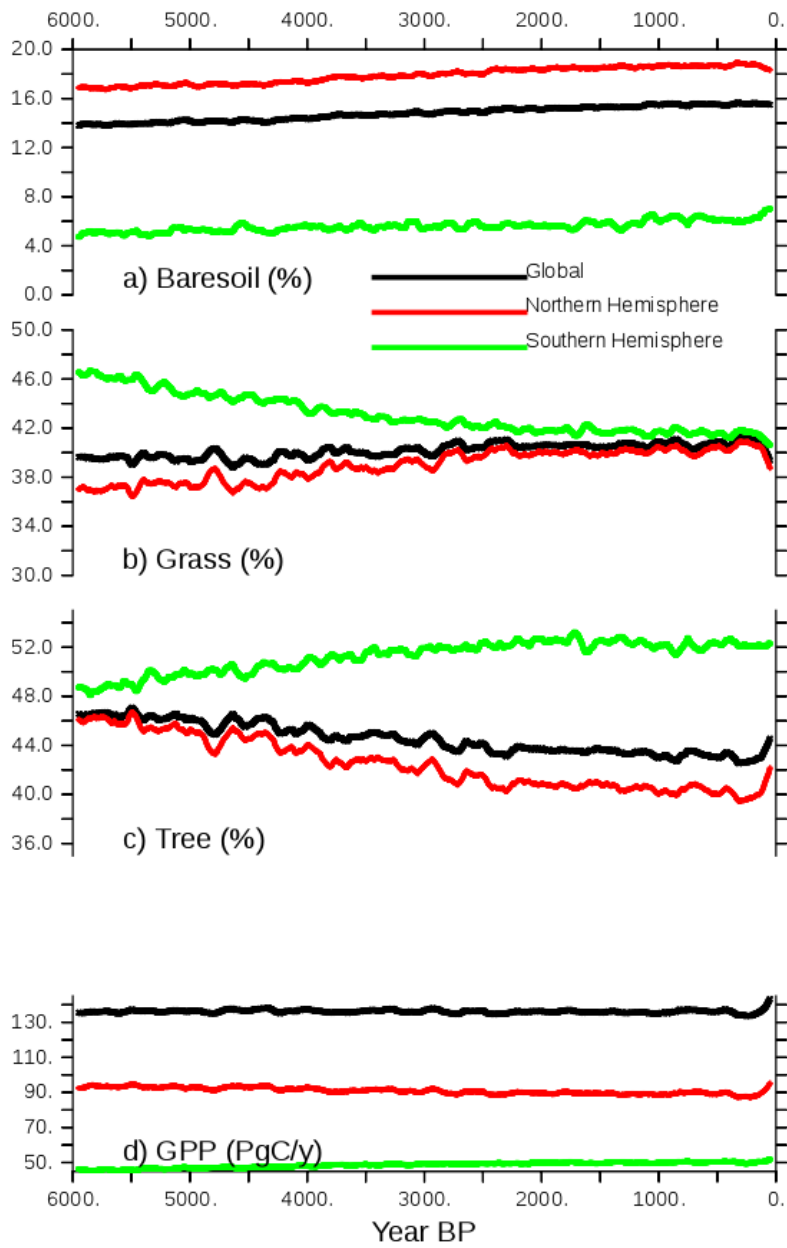


Figure 9:

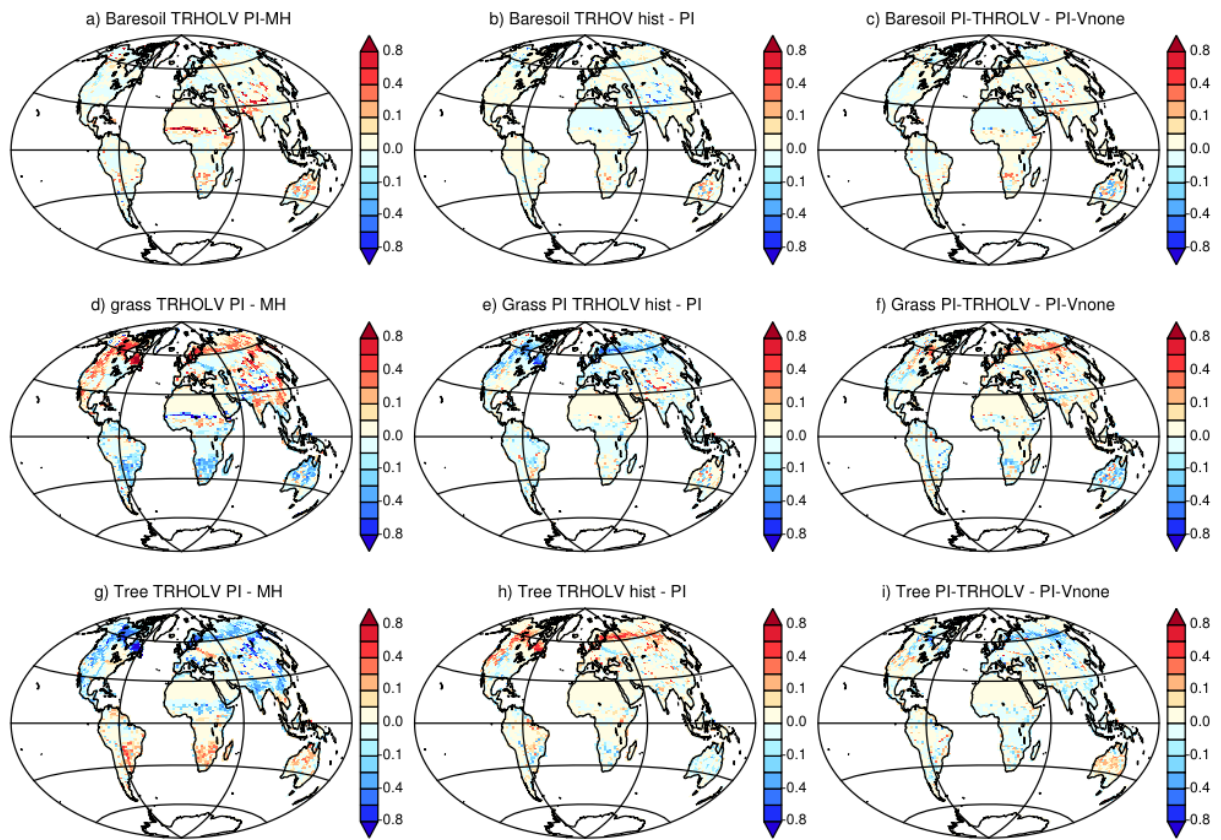


Figure 10.

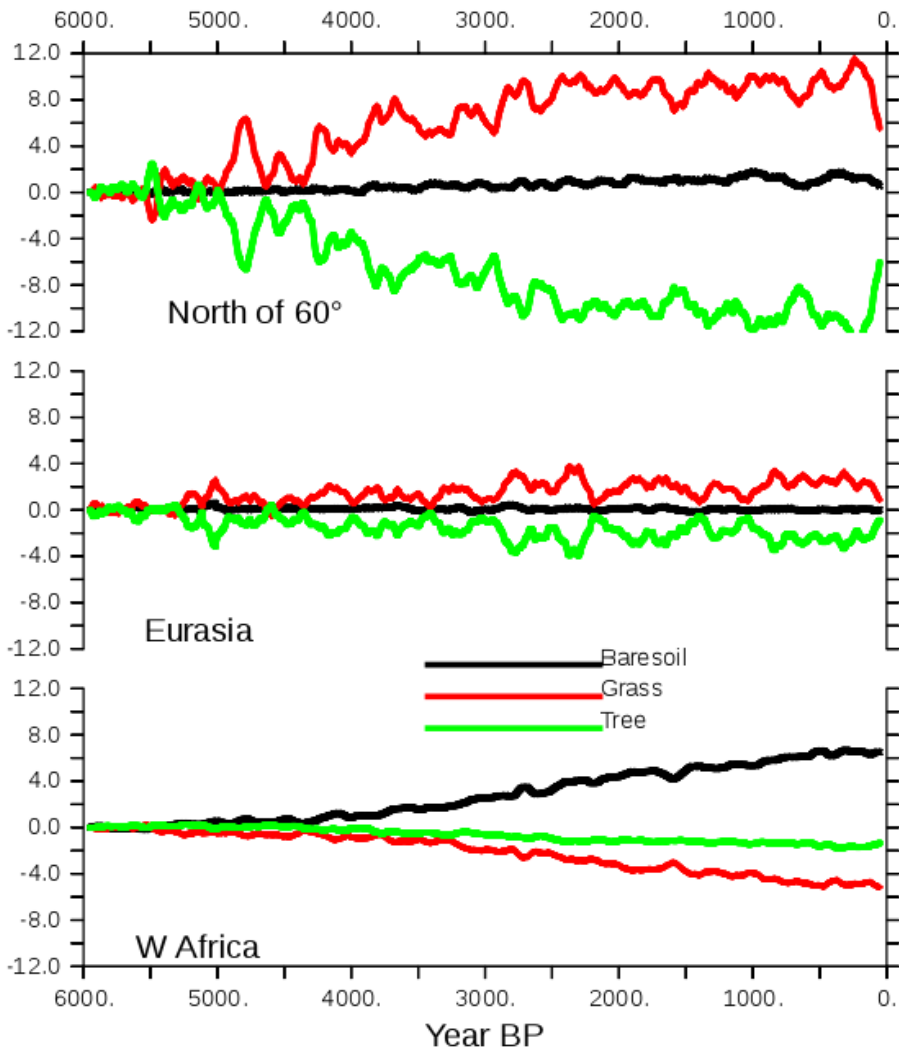


Figure 11:

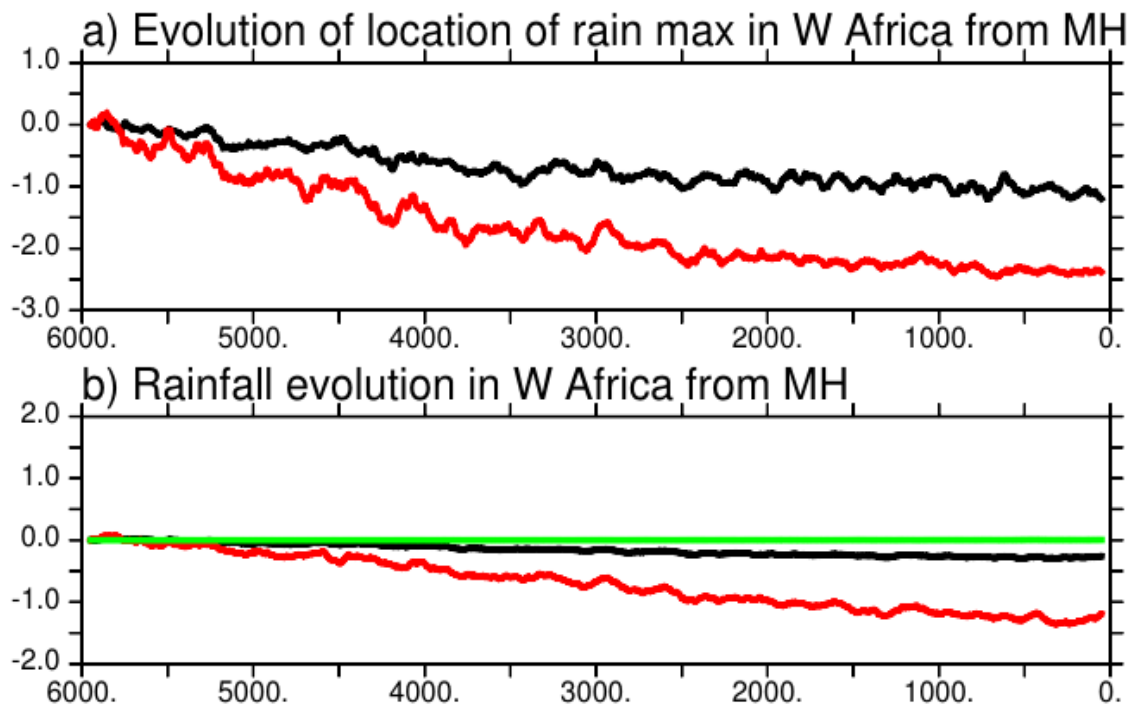


Figure 12.

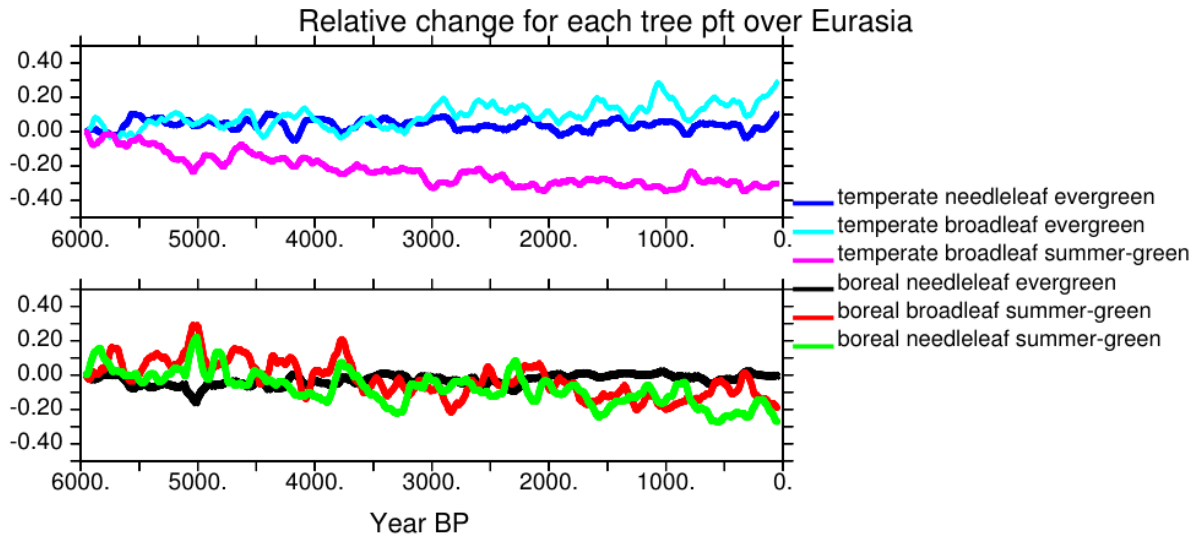


Figure 13:

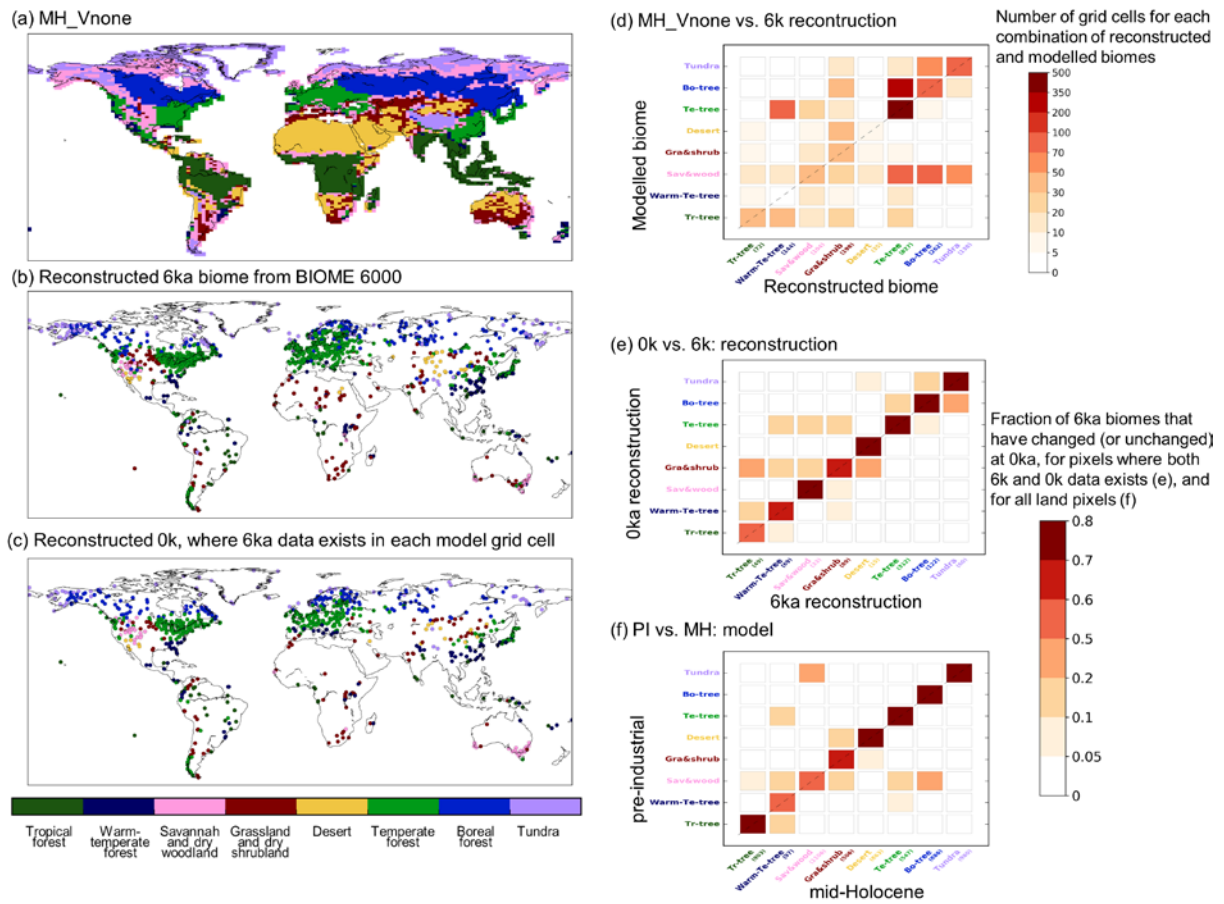


Figure 14:

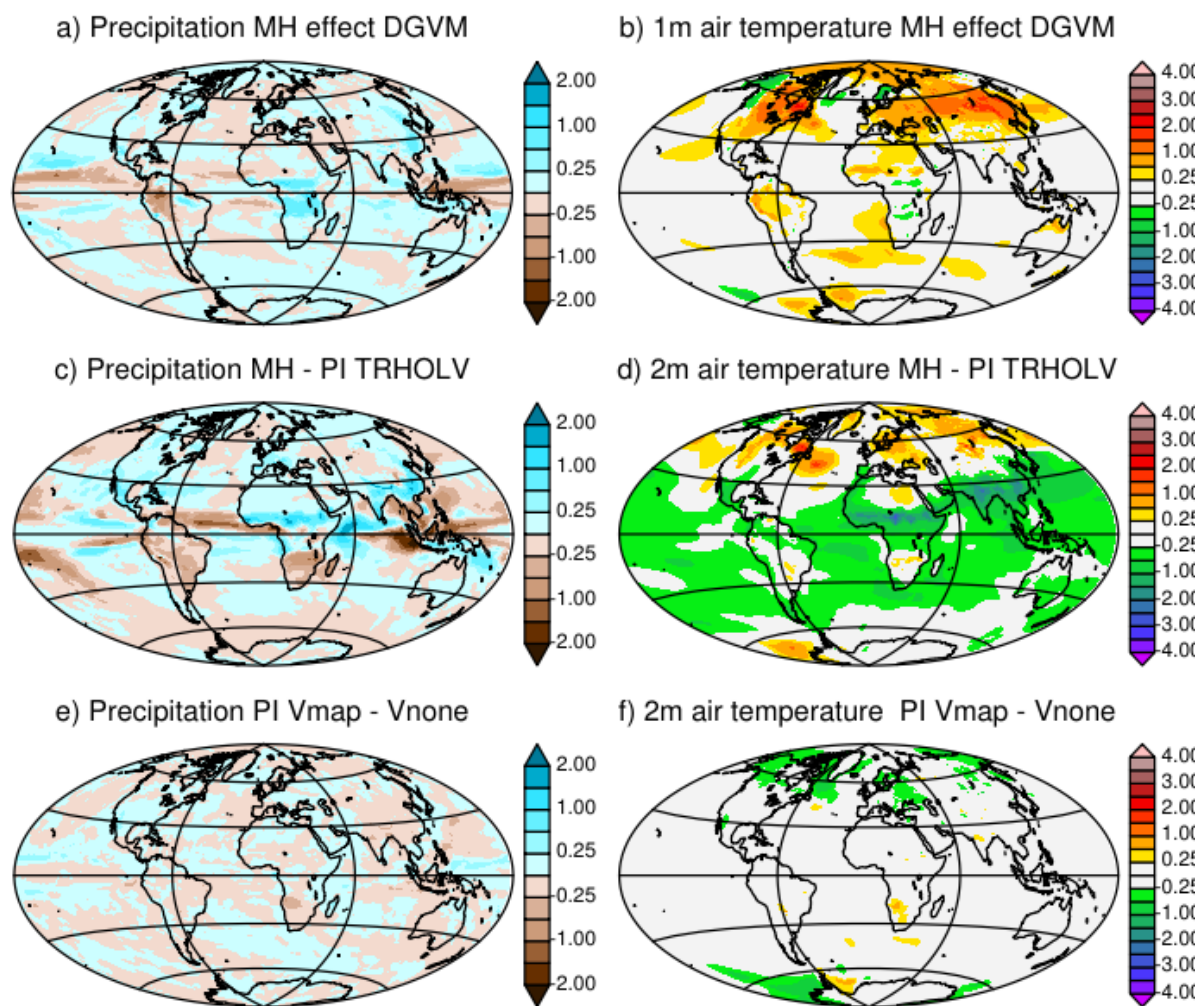


Figure 15:

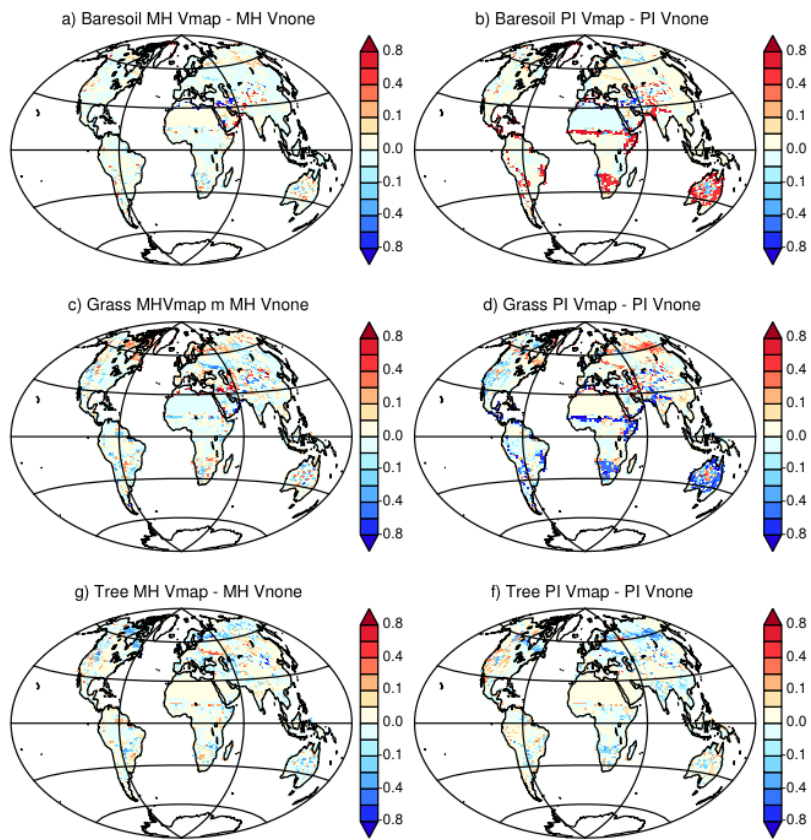


Figure 16:

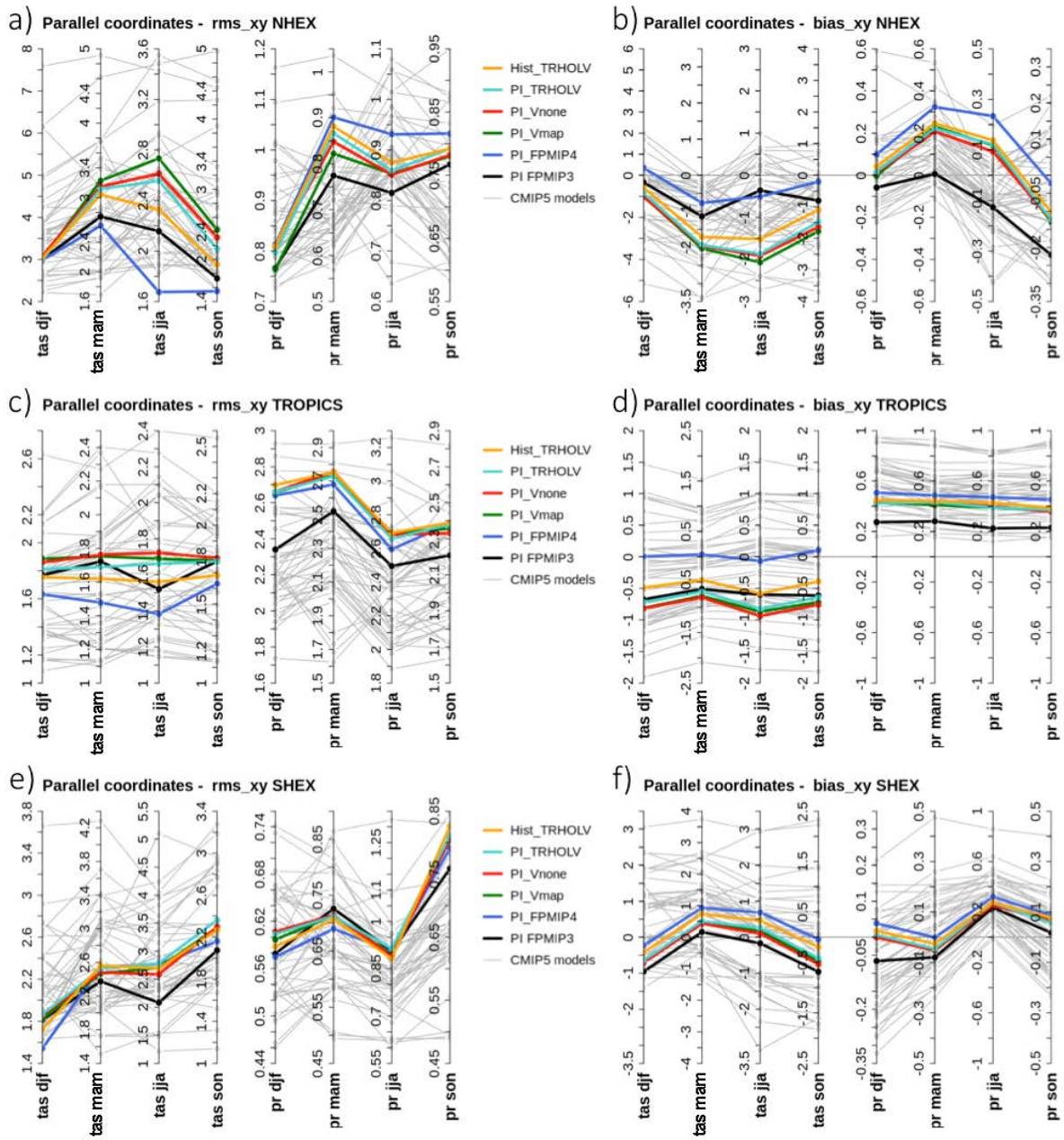
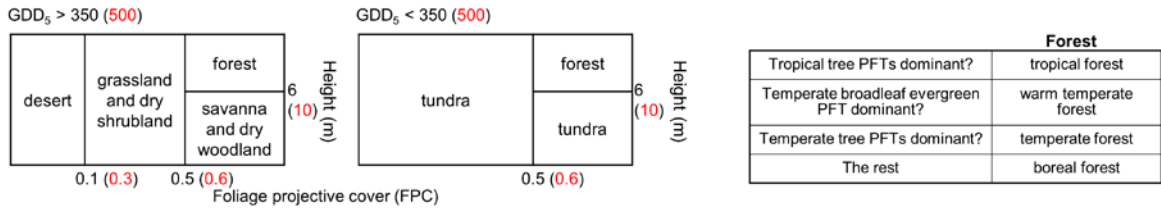
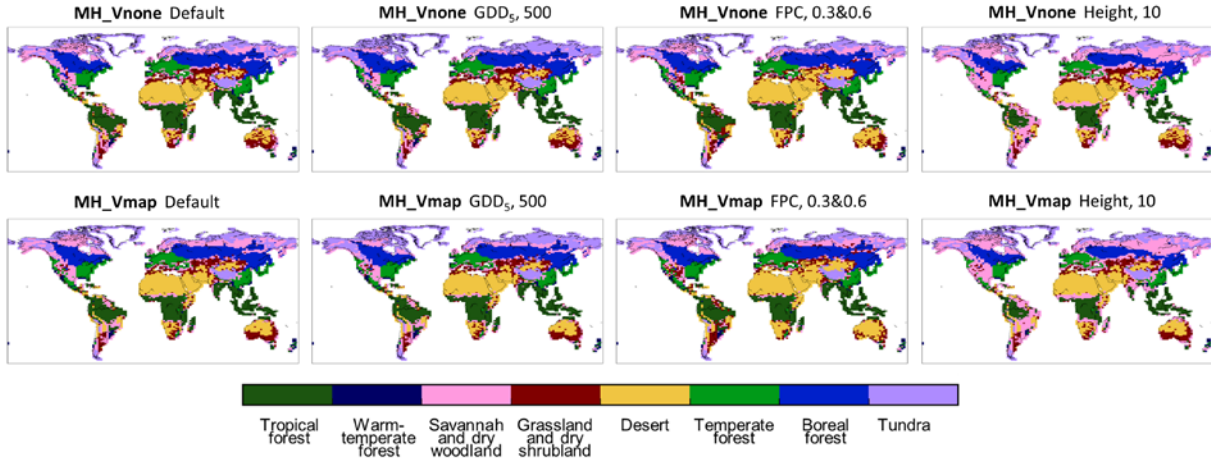


Figure A1:

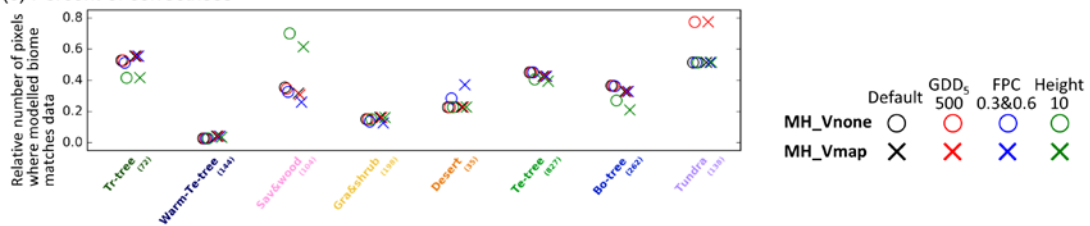
(a) Algorithm to convert the modelled PFT properties into the 8 mega-biomes provided by BIOME 6000



(b) Simulated mega-biome distribution



(c) Percent of correctness



(d) Percent of correctness, TRHOLV (100 years BP)

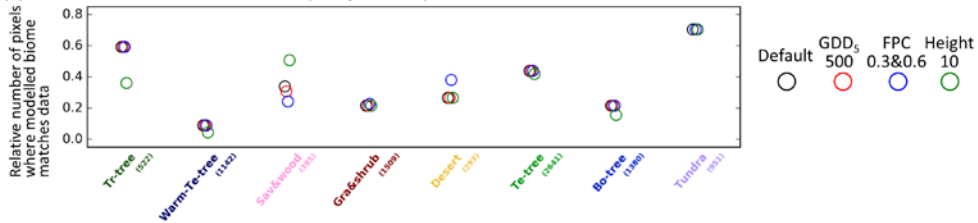


Figure A2 :

